



This is a repository copy of *3-D local mesh refinement XFEM with variable-node hexahedron elements for extraction of stress intensity factors of straight and curved planar cracks*.

White Rose Research Online URL for this paper:
<http://eprints.whiterose.ac.uk/106281/>

Version: Accepted Version

Article:

Wang, Z., Yu, T., Bui, T.Q. et al. (4 more authors) (2017) 3-D local mesh refinement XFEM with variable-node hexahedron elements for extraction of stress intensity factors of straight and curved planar cracks. *Computer Methods in Applied Mechanics and Engineering*, 313. pp. 375-405. ISSN 0045-7825

<https://doi.org/10.1016/j.cma.2016.10.011>

Article available under the terms of the CC-BY-NC-ND licence
(<https://creativecommons.org/licenses/by-nc-nd/4.0/>)

Reuse

This article is distributed under the terms of the Creative Commons Attribution-NonCommercial-NoDerivs (CC BY-NC-ND) licence. This licence only allows you to download this work and share it with others as long as you credit the authors, but you can't change the article in any way or use it commercially. More information and the full terms of the licence here: <https://creativecommons.org/licenses/>

Takedown

If you consider content in White Rose Research Online to be in breach of UK law, please notify us by emailing eprints@whiterose.ac.uk including the URL of the record and the reason for the withdrawal request.



eprints@whiterose.ac.uk
<https://eprints.whiterose.ac.uk/>

Accepted Manuscript

3-D local mesh refinement XFEM with variable-node hexahedron elements for extraction of stress intensity factors of straight and curved planar cracks

Zhen Wang, Tiantang Yu, Tinh Quoc Bui, Satoyuki Tanaka, Chuanzeng Zhang, Sohichi Hirose, Jose L. Curiel-Sosa

PII: S0045-7825(16)31306-8

DOI: <http://dx.doi.org/10.1016/j.cma.2016.10.011>

Reference: CMA 11172

To appear in: *Comput. Methods Appl. Mech. Engrg.*

Received date: 12 February 2016

Revised date: 11 August 2016

Accepted date: 4 October 2016

Please cite this article as: Z. Wang, T. Yu, T.Q. Bui, S. Tanaka, C. Zhang, S. Hirose, J.L. Curiel-Sosa, 3-D local mesh refinement XFEM with variable-node hexahedron elements for extraction of stress intensity factors of straight and curved planar cracks, *Comput. Methods Appl. Mech. Engrg.* (2016), <http://dx.doi.org/10.1016/j.cma.2016.10.011>

This is a PDF file of an unedited manuscript that has been accepted for publication. As a service to our customers we are providing this early version of the manuscript. The manuscript will undergo copyediting, typesetting, and review of the resulting proof before it is published in its final form. Please note that during the production process errors may be discovered which could affect the content, and all legal disclaimers that apply to the journal pertain.



Research Article:

3-D Local Mesh Refinement XFEM with Variable-Node Hexahedron
Elements for Extraction of Stress Intensity Factors of Straight and Curved
Planar Cracks

Zhen Wang^a, Tiantang Yu^{a,*,#}, Tinh Quoc Bui^{b,c,*,†}, Satoyuki Tanaka^d,
Chuanzeng Zhang^e, Sohichi Hirose^c, Jose L. Curiel-Sosa^f

^aDepartment of Engineering Mechanics, Hohai University, Nanjing 211100, PR China.

^bInstitute for Research and Development, Duy Tan University, Da Nang City, Vietnam

^cDepartment of Mechanical and Environmental Informatics, Tokyo Institute of Technology,
2-12-1-W8-22, Ookayama, Meguro-ku, Tokyo 152-8552, Japan.

^dGraduate School of Engineering, Hiroshima University, Higashi-Hiroshima 739-8527, Japan

^eDepartment of Civil Engineering, University of Siegen, Germany

^fDepartment of Mechanical Engineering, The University of Sheffield, Sir Frederick Mappin
Building, Mappin Street, S1 3JD Sheffield, United Kingdom

*Corresponding authors: Duy Tan University, Da Nang City, Vietnam & Tokyo Institute of Technology, Japan
(T.Q. Bui); Hohai University, Nanjing, PR China (T.T. Yu)

Tel.: +81 (03) 57343587 (T.Q. Bui); Tel.: +86 (25) 52430342(T.T. Yu)

#E-mail: tiantangyu@hhu.edu.cn (T.T. Yu)

†E-mail: buiquoctinh@duytan.edu.vn; tinh.buiquoc@gmail.com (T. Q. Bui)

Abstract

A novel local mesh refinement approach for failure analysis of three-dimensional (3-D) linear elastic solids is developed, considering both 3-D straight and curved planar cracks. The present local mesh refinement formulation is in terms of the extended finite element methods and variable-node hexahedron elements, driven by a *posteriori* error indicator. Our 3-D formulation using hexahedron elements rigorously embraces a *posteriori* error estimation scheme, a structural coupling scale-meshes strategy and an enrichment technique. Remeshing is only performed where it is needed, e.g., a vicinity of crack, through an error estimator based on the recovery stress procedure. To treat the mismatching problem induced by different scale-meshes in the domain, a structural coupling scheme employing variable-node transition hexahedron elements based on the generic point interpolation with an arbitrary number of nodes on each of their faces is presented. The 3-D finite element approximations of field variables are enhanced by enrichments so that the mesh is fully independent of the crack geometry. The displacement extrapolation method is taken for the evaluation of linear elastic fracture parameters (e.g., stress intensity factors - SIFs). To show the accuracy and performance of our 3-D proposed formulation, six numerical examples of planar 3-D straight and curved shaped cracks with single and mixed-mode fractures and different configurations are considered and analyzed. The SIFs computed by the developed method are validated with respect to analytical solutions and the ones derived from the conventional XFEM. Associated with an adaptive process, the present 3-D formulation allows the analysts to gain a desirable accuracy with a few trials, which is suited for practices purpose.

Keywords: *Fracture; XFEM; Error estimation; Adaptive; Variable-node element; 3D cracks; Hexahedron element.*

1. Introduction

Over the past few decades, studies on the numerical computations of fracture phenomena of materials and structures has progressed significantly, which have had a tremendous impact on engineering practice and design. Defects or cracks whose existence in structures is unavoidable have a strong effect on the integrity and performance of engineering materials and structures. Major cracks in structures must be fully considered to evaluate the residual strength of cracked structures, which could essentially provide valuable information and knowledge to the designers to mitigate the detrimental effects caused by cracks. Compared with the size of structures, the geometry of crack is often small, and in order to represent the geometry of such a crack, a fine mesh discretized for the cracked area is usually made. However, the computation for that is obviously time-consuming, especially if the whole structure in 3-D discretized by a fine mesh is taken. In some particular cases, the computational tasks even can not be conducted successfully. The costs may be saved significantly if a coarser mesh is used for region without cracks. As a result, a domain that comprises both fine and coarse meshes induces the mismatching problem of different meshes, and an appropriate technique to couple the fine and coarse meshes is hence needed.

Furthermore, another important problem that is often encountered in the vicinity of crack, particularly near crack-tip, is the high gradients [1-3]. Modeling the high gradients using mesh-based methods usually requires a fine mesh in the vicinity of crack. Therefore, accurate solutions obtained by utilizing mesh-based methods (e.g., finite elements) are the results derived from a model in which a fine mesh around the crack is used, while a coarser mesh is for the rest of the body. The use of different meshes in such high gradient model also causes the mismatching problems, and a structural coupling technique to link the meshes at different levels is mandatory.

The numerical difficulty for the adoption of a non-uniform mesh is the treatment of transition elements which have hanging nodes. Numerous special techniques have been developed for treating the mismatching problems caused by different meshes such as the Lagrange multipliers [4], projection method [5], penalty function parameters [6], mortar method [7], Arlequin method [8]. Belytschko et al. [9] introduced a multiscale aggregating discontinuity method to treat the discontinuity at macroscale level via the extended finite

element method (XFEM) [10]. The underlying characteristic of their model lies in the treatment of material instabilities occurring in the micromodel, while an equivalent discontinuity is injected into the macromodel. The method was then applied to the analysis of micro-macro failure of composites [11, 12]. Plews and Duarte [13] developed a bridging multiple structural scales aimed at resolving the challenging multiscale phenomena within the framework of the generalized FEM with global-local enrichment functions. Loehnert and Belytschko [5] reported an interesting work that combines the multiscale projection method and the XFEM for 2-D macrocrack/microcrack at different length scales. With the aid of the projection method, the resulting fine-scale stress fields are hence estimated onto the coarse-scale. There are several other multiscale models available in literature, e.g., see Refs. [14-18], and the underlying idea of those methods is to impose constraints at nodes on mismatching interfaces to connect different scale meshes. Those methods however often require some modifications on the system matrix whenever the constraints are imposed [19]. Kumar et al. [20, 21] proposed a homogenized XFEM to simulate fatigue crack growth and a virtual node XFEM to represent kinked cracks based on a non-uniform mesh. In order to ensure the continuity in the displacement fields, six-node and five-node transition elements were developed, respectively.

Recently, the variable-node transition elements [19, 22], which have an arbitrary number of nodes on the element sides and faces, are developed based on the generic point interpolation for solving engineering problems. By using the variable-node elements, the mismatching interfaces are converted into matching interfaces in a straightforward manner, thus the system matrix does not need to be modified, an effective feature that does not valid in some of the previous methods.

In light of XFEM developments, the authors have recently applied the XFEM to fracture mechanics problems in multiphase homogeneous and nonhomogeneous functional smart composite materials under static, dynamic and thermal coupled electromechanical loading conditions, e.g., see Refs.[23-28]. Fatigue crack growth of interfacial cracks in bi-layered functionally graded materials is also studied using the XFEM [29]. Recently, XFEM simulation for cohesive crack growth in concrete structures with two new solution algorithms is presented [30]. A stabilized discrete shear gap extended element is developed for cracked Mindlin plates considering distorted mesh [31] and cracked functionally graded plates [32]. The XFEM for

hydraulic fracturing in rock mass is analyzed in [33]. More recently, the authors proposed an enhanced XFEM using consecutive-interpolation procedure for accurately extracting stress intensity factors as detailed in [34]. The authors have found that the standard XFEM is well suited for modeling problems with non-smoothed solutions but to make the method more flexible and effective in practical applications, we devote our motivation to the novel approach that is reported in the present manuscript.

It is believed that the determination of accurate fracture parameters of straight or curved cracks in 3-D configurations with mixed-mode loading remains a great challenge in the computational fracture mechanics. Pathak et al. [35] proposed a simple and efficient XFEM approach for 3-D cracks. A crack front is divided into a number of piecewise curve segments to avoid an iterative solution. In crack front elements, the level set functions are approximated by higher order shape functions which assure the accurate modeling of the crack front. Later, they applied the method to model fatigue crack growth simulations of 3-D problems [36, 37]. Sharma et al. [38] employed XFEM to obtain the stress intensity factors of a semi-elliptical part through thickness axial crack. Level set functions are approximated using higher order shape functions in the crack front elements to ensure the accurate modeling of the crack. This paper particularly focuses on the development of an effective and accurate local mesh refinement XFEM (Lm-XFEM) using hexahedron elements to accurately estimate linear elastic fracture parameters of both planar 3-D straight and curved cracks. The proposed approach runs with an engine embracing three components of tackling different tasks, an adaptation algorithm for local mesh refinement, an enrichment scheme for capturing the cracks, and a coupling method for treating mismatching meshes in the model.

In the present Lm-XFEM formulation, an adaptive algorithm whose role is to refine the elements is required. The elements to be refined have been detected by a *posteriori* error estimation algorithm. The adaptive procedure using a *posteriori* error estimation in terms of the XFEM is adopted from the work done by Prange et al. [3]. The Zienkiewicz and Zhu error estimator [39] is used and that is based on a stress smoothing technique. The enhanced smoothed stresses incorporating the discontinuities and singularities induced by cracks are recovered, by which the error estimation for arbitrary distributed cracks can be made. It is noted that every stress component is recovered separately and the nodal enhanced smoothed stresses

are recovered with a least square fit. An error indicator applied to subsequently refined meshes is gained with a relative error, and every element with a relative error exceeds a given specified value of tolerance error is then refined with a set of subdivision elements. For further information, interested readers can refer to [2, 3, 18].

The Lm-XFEM utilizing the variable-node hexahedron elements [19, 22] with an arbitrary number of nodes on each of their faces is to couple the meshes at different levels; while the enrichment scheme [10, 40] for describing the discontinuities induced by the crack surfaces and the singularities because of crack front is taken. Notice that the variable-node hexahedron elements [19, 22] are further extended to carry cracks in this work. In fact, unlike the problems with smoothed solutions, the problems under investigation involving cracks (or non-smoothed solutions type) require not only a regular variable-node element, but also a variable-node element that can carry crack. As can be seen in the subsequent sections the variable-node hexahedron elements can be cut by a crack or contain a crack-tip, which do exist in the present model. Therefore, such cut and crack-tip variable-node hexahedron transition elements must be developed as well to fully assure the compatibility of the configuration, the convergence of the solutions or avoid the undesirable behaviors.

The Lm-XFEM enables one to utilize a refined mesh only in the vicinity of the crack where it is required, and the matching interfaces between different meshes are directly obtained. Therefore, small crack sizes can be considered in the analysis of the whole large structures and the accuracy of the solutions around the cracks can be significantly improved with a low cost. More importantly the accuracy of the results is controllable.

It is also worth noting that the traditional fixed-node element is one special case for the variable-node elements, hence the variable-node hexahedron elements can be implemented within an existing 3-D XFEM computer code with little modification and effort. The Lm-XFEM associated with an adaptive process allows the users to achieve desired accuracies with some trials. Another important point is that each node of the variable-node hexahedron element has its own degree of freedom and a symmetric system matrix is constructed in the same way as the standard FEM [19].

It is known that the most important characterizing fracture parameters to represent the strength of the singular fields at the crack tips in 2-D and crack front in 3-D are the stress

intensity factors (SIFs). Several well-known methods have been proposed to determine the SIFs, and in this paper the displacement extrapolation method near the crack tip [41] is adopted for our 3-D straight and curved cracks. We will again discuss this issue a bit more detail in the subsequent sections. Basically, the displacement extrapolation method can be used for direct evaluation of the SIFs according to the relative crack surface displacements.

It is very important to mention here that our aim is to develop a novel effective local mesh refinement in terms of XFEM for the simulation of cracks in 3-D, and thus this paper does not devote to a micro-macro multiscale failure analysis. A misleading/misunderstanding of multiscale failure of solids in terms of homogenization frame however should be avoided.

The body of paper is structured as follows. In Section 2, the 3-D Lm-XFEM formulation is presented in which the variable-node hexahedron elements to link the different scale elements, a posteriori recovery-based error estimator for the adaptive purpose, numerical integration, enriched displacement approximations, etc. are detailed. Computation of 3-D stress intensity factors (SIFs) using the displacement extrapolation method is briefly described in Section 3. Numerical examples are analyzed and discussed in Section 4, and some conclusions and outlook drawn from the study are given in Section 5.

2. Formulation of three-dimensional local mesh refinement XFEM

2.1 Enriched finite element approximation

The underlying idea of the XFEM is that the standard finite element approximation is locally enriched by additional functions based on the partition of unity to model the discontinuities to be independent of the meshes. For a cracked medium, the extended displacement approximation can be written as [10]

$$\mathbf{u}^h(\mathbf{x}) = \sum_{i \in N^s} N_i(\mathbf{x}) \mathbf{u}_i + \sum_{j \in N^{\text{cut}}} N_j(\mathbf{x}) [H(\mathbf{x}) - H(\mathbf{x}_j)] \mathbf{a}_j + \sum_{k \in N^{\text{tip}}} N_k(\mathbf{x}) \sum_{\alpha=1}^4 [F_\alpha(\mathbf{x}) - F_\alpha(\mathbf{x}_k)] \mathbf{b}_{k\alpha} \quad (1)$$

where \mathbf{u}_i is the vector of nodal degrees of freedom defined in standard finite elements, \mathbf{a}_j and $\mathbf{b}_{k\alpha}$ are the vectors of nodal enrichment variables; $N_i(\mathbf{x})$ denote the standard finite element shape functions. Because of the enrichment, the discretized nodes of entire domain are generally categorized into three different sets: (a) N^s defines the set of all nodes in the

discretization; (b) N^{cut} is the set of nodes whose basis function support is entirely split by the crack and are enriched with a discontinuous Heaviside function $H(\mathbf{x})$. The function takes on the value +1 above the crack and -1 below the crack; and (c) N^{tip} is the last one that defines the set of nodes enriched with the asymptotic crack-tip enrichment functions $F_\alpha(\mathbf{x})$ ($\alpha = 1, \dots, 4$). The set N^{tip} represents the set of nodes whose basis function support is partly split by the crack.

To model the crack front and to represent the crack-tip fields in 3-D isotropic elasticity computation, the 2-D crack-tip branch enrichment functions $F_\alpha(\mathbf{x})$ are used in elements which contain the crack front, and are given by

$$[F_\alpha(\mathbf{x}), \alpha = 1, \dots, 4] = \left[\sqrt{r} \sin \frac{\theta}{2} \quad \sqrt{r} \cos \frac{\theta}{2} \quad \sqrt{r} \sin \frac{\theta}{2} \sin \theta \quad \sqrt{r} \cos \frac{\theta}{2} \sin \theta \right] \quad (2)$$

where r and θ are the crack-tip polar co-ordinates.

In XFEM, crack surfaces are often described by using the level sets. Two signed distance functions are defined to describe a 3-D crack. Two iso-zero level sets can define the crack location, and the enrichment type of each node can be determined according to the value of nodal level set function [42]. Sukumar et al. [40] discussed the computational geometry issues associated with the representation of the crack and the enrichment of the finite element approximation in detail.

Remark #1: It is important to point out here that the 2-D crack-tip branch enrichments in Eq. (2) are also valid for 3-D crack problems. Preceding studies [40, 42] already indicate that the asymptotic fields are two-dimensional in nature in the neighborhood of the crack front in 3-D problems. Also notice that only the first term of the enrichment functions is discontinuous while others are added to enhance the accuracy in elastic fracture mechanics problems. The 2-D branch functions in Eq. (2) span the near-tip asymptotic solutions for an elastic crack in two dimensions, and more importantly, Sukumar et al. [40] and Moës et al. [42] have found that such 2-D basis to be quite adequate accuracy for 3-D crack problems.

Remark #2: Blending elements do exist in the displacement approximation shown in Eq. (1). Blending elements in the XFEM may reduce the overall convergence rate as stated in [43]. Some approaches have been proposed to treat the blending elements, and these approaches may be divided into four categories: corrected or weighted XFEM [44, 45], suppressing blending

elements by coupling enriched and standard regions [43, 46], hierarchical shape functions in blending elements [47], and assumed strain blending elements [48]. In this study, the blending element issue is not considered, but it would be a potential work for our future study.

2.2 Linkage meshes technique using variable-node transition elements

One layer of variable-node transition elements exists between two different scale elements as schematically represented in yellow in Fig. 1 for hexahedron elements. The variable-node elements [19], which have an arbitrary number of nodes on the element faces, with special bases that have slope discontinuities in 3-D domains, and the elements retain the linear interpolation between any two neighboring nodes. As stated by Sohn et al. [19] or Lim et al. [22] that the variable-node elements can provide a flexibility to resolve non-mismatching mesh problems like the mesh connection and adaptive mesh refinement. It hence motivates us to adopt the variable-node elements to solve the mismatching problems of different scale meshes in the present formulation.

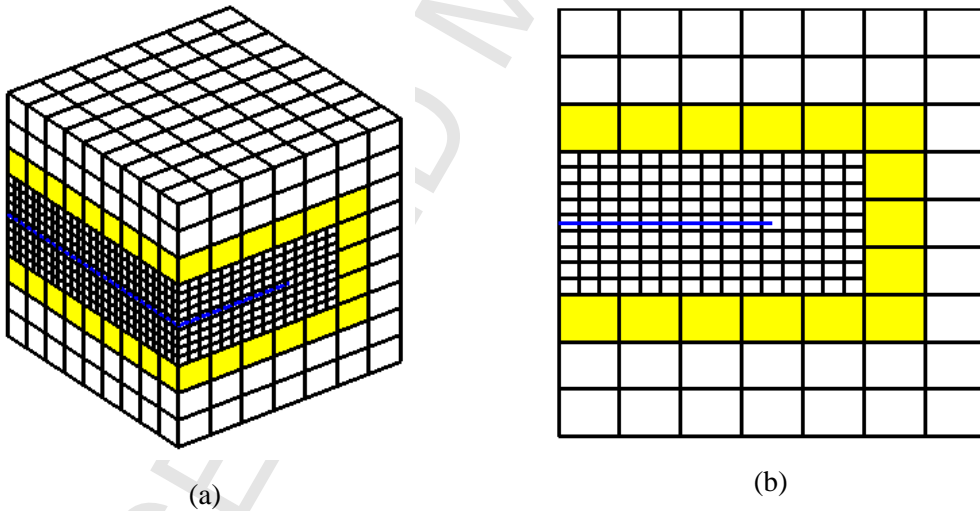


Fig. 1 Hexahedral meshes discretization of a straight edge crack in a 3-D solid containing two different scale hexahedron elements (a). Schematically showing one layer of variable-node transition hexahedron elements connected two different meshes as marked in yellow and its front view (b). The blue line represents the crack.

Let us consider the approximate displacements $\mathbf{u}^h(\boldsymbol{\xi})$ for $\mathbf{u}(\boldsymbol{\xi})$ by the point interpolation,

with N_p based-polynomials, $\mathbf{u}^h(\xi)$ can then be expressed as follows:

$$\mathbf{u}^h(\xi) = \sum_{i=1}^{N_p} N_i(\xi) \mathbf{u}_i = \mathbf{a}^T \mathbf{p}(\xi) \quad (3)$$

where N_p is the number of sampling points in the point interpolation;

$$N_i = \begin{bmatrix} N_i & 0 & 0 \\ 0 & N_i & 0 \\ 0 & 0 & N_i \end{bmatrix} \quad (4)$$

is the shape function matrix, in which N_i is the shape function that is associated with node i ;

$\mathbf{u}_i = [u_i \ v_i \ w_i]^T$ is the nodal variable vector; \mathbf{a}^T is the $3 \times N_p$ matrix of the unknown coefficients while $\mathbf{p}(\xi)$ is the $N_p \times 1$ column vector of the polynomial basis.

For the eight-node hexahedron element, the polynomial basis can be given by

$$\mathbf{p}(\xi) = [1 \ \xi \ \eta \ \zeta \ \xi\eta \ \eta\zeta \ \xi\zeta \ \xi\eta\zeta]^T \quad (5)$$

where ξ , η and ζ are the local coordinates in the isoparametric element.

The point interpolation follows that is then expressed as

$$\mathbf{u}^h(\xi) = \mathbf{a}^T \mathbf{p}(\xi) = \mathbf{U}^T \mathbf{q} \mathbf{p}(\xi) \quad (6)$$

with

$$\mathbf{q} = [p_1 \ \dots \ p_8] \quad (7)$$

$$\mathbf{U}^T = [\mathbf{u}_1 \ \dots \ \mathbf{u}_8] \quad (8)$$

From Eqs. (3) to (8), the shape functions of the eight-node hexahedron element are obtained and are written in general form as

$$N_i(\xi) = \frac{1}{8} (1 + \xi \xi_i) (1 + \eta \eta_i) (1 + \zeta \zeta_i) \quad (9)$$

By adding some extra special basis to meet the point interpolation characteristics, variable-node elements can then be generated. Basically, the choice for the extra special basis often depends on the interpolation type that is required on the element-surfaces. A linear variable-node hexahedron element, that is called as a $(8+j+k+l+p+q+r)$ -node element, all nodes can be divided into 7 types as follow: Type 1: 8 corner nodes of the hexahedron element; Type 2: j nodes on the edges of $\xi = \pm 1$, $\eta = \pm 1$, and $\zeta \neq \pm 1$; Type 3: k additional nodes on the

edges of $\eta = \pm 1$, $\zeta = \pm 1$, and $\xi \neq \pm 1$; Type 4: l additional nodes on the edges of $\xi = \pm 1$, $\zeta = \pm 1$, and $\eta \neq \pm 1$; Type 5: p additional nodes on the surfaces of $\xi = \pm 1$; Type 6: q additional nodes on the surfaces of $\eta = \pm 1$; and Type 7: r additional nodes on the surfaces of $\zeta = \pm 1$. They are schematically depicted in Fig. 2. The polynomial basis can be given by

$$\begin{aligned}
\mathbf{p}(\xi) = & [1, \xi, \eta, \zeta, \xi\eta, \eta\zeta, \xi\zeta, \xi\eta\zeta, (\xi + \text{sign}(\xi_0))(\eta + \text{sign}(\eta_0))|\zeta - \zeta_0|, \dots, \\
& (\xi + \text{sign}(\xi_{8+j}))(\eta + \text{sign}(\eta_{8+j}))|\zeta - \zeta_{8+j}|, |\xi - \xi_{8+j+1}|(\eta + \text{sign}(\eta_{8+j+1}))(\zeta + \text{sign}(\zeta_{8+j+1})), \dots, \\
& |\xi - \xi_{8+j+k}|(\eta + \text{sign}(\eta_{8+j+k}))(\zeta + \text{sign}(\zeta_{8+j+k})), (\xi + \text{sign}(\xi_{8+j+k+1}))|\eta - \eta_{8+j+k+1}|(\zeta + \text{sign}(\zeta_{8+j+k+1})), \dots, \\
& (\xi + \text{sign}(\xi_{8+j+k+l}))|\eta - \eta_{8+j+k+l}|(\zeta + \text{sign}(\zeta_{8+j+k+l})), (\xi + \text{sign}(\xi_{8+j+k+l+1}))|\eta - \eta_{8+j+k+l+1}|(\zeta - \zeta_{8+j+k+l+1}), \dots, \\
& (\xi + \text{sign}(\xi_{8+j+k+l+p}))|\eta - \eta_{8+j+k+l+p}|(\zeta - \zeta_{8+j+k+l+p}), |\xi - \xi_{8+j+k+l+p+1}|(\eta + \text{sign}(\eta_{8+j+k+l+p+1}))|\zeta - \zeta_{8+j+k+l+p+1}|, \dots, \\
& |\xi - \xi_{8+j+k+l+p+q}|(\eta + \text{sign}(\eta_{8+j+k+l+p+q}))|\zeta - \zeta_{8+j+k+l+p+q}|, |\xi - \xi_{8+j+k+l+p+q+1}|(\eta - \eta_{8+j+k+l+p+q+1}), \\
& (\zeta + \text{sign}(\zeta_{8+j+k+l+p+q+1})), \dots, |\xi - \xi_{8+j+k+l+p+q+r}|(\eta - \eta_{8+j+k+l+p+q+r})|\zeta + \text{sign}(\zeta_{8+j+k+l+p+q+r})]^\top \quad (10)
\end{aligned}$$

The corresponding $\mathbf{q} = \mathbf{p}(\xi_i)$ and \mathbf{U}^\top are given by

$$\mathbf{U}^\top = \begin{bmatrix} \mathbf{u}_1 & \dots & \mathbf{u}_i & \dots & \mathbf{u}_{8+j+k+l+p+q+r} \end{bmatrix} \quad (11)$$

From Eq. (5), the shape functions of the $(8+j+k+l+p+q+r)$ -node element can be obtained as

$$[N_1, \dots, N_{8+j+k+l+p+q+r}]^\top = \mathbf{q}^{-1} \mathbf{p}(\xi) \quad (12)$$

Furthermore, the shape functions of a typical 3-D variable 13-node hexahedron element are depicted in Fig. 3. It is noted that the shape functions at each node possess the Kronecker's delta function property.

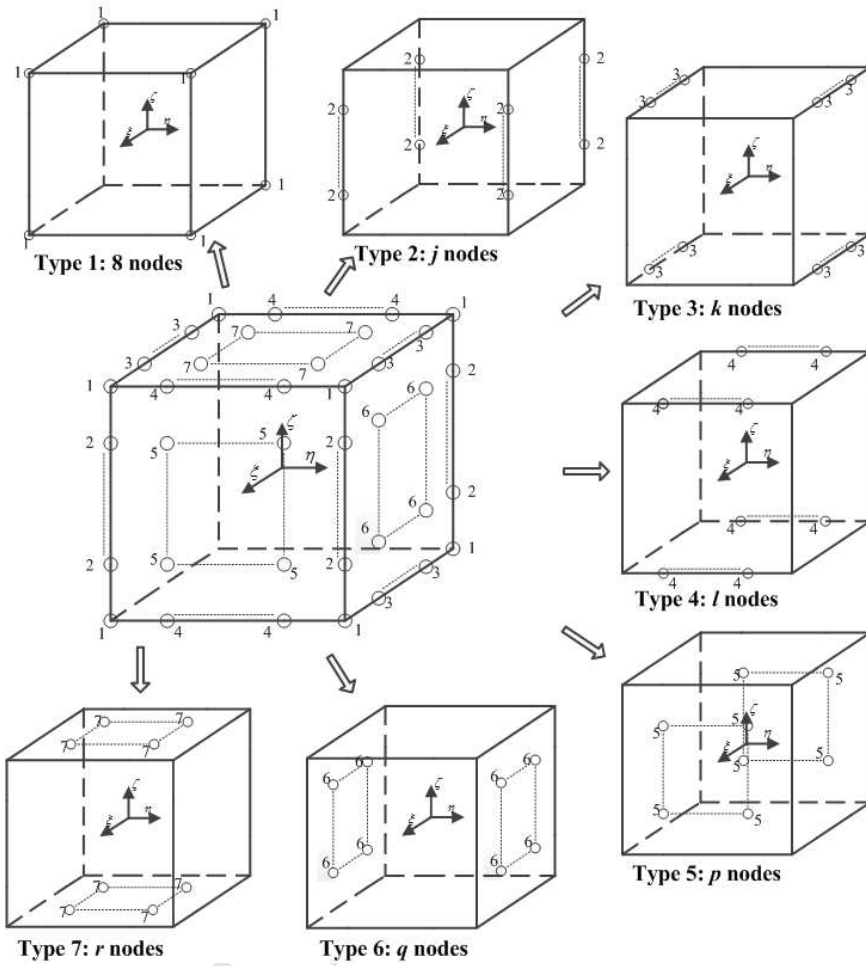
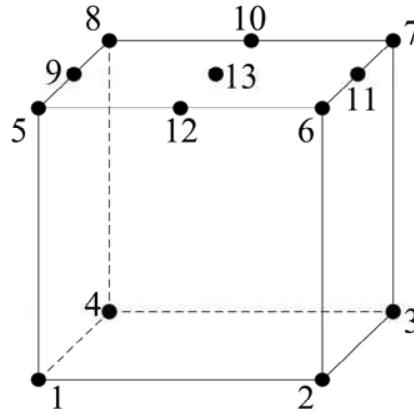
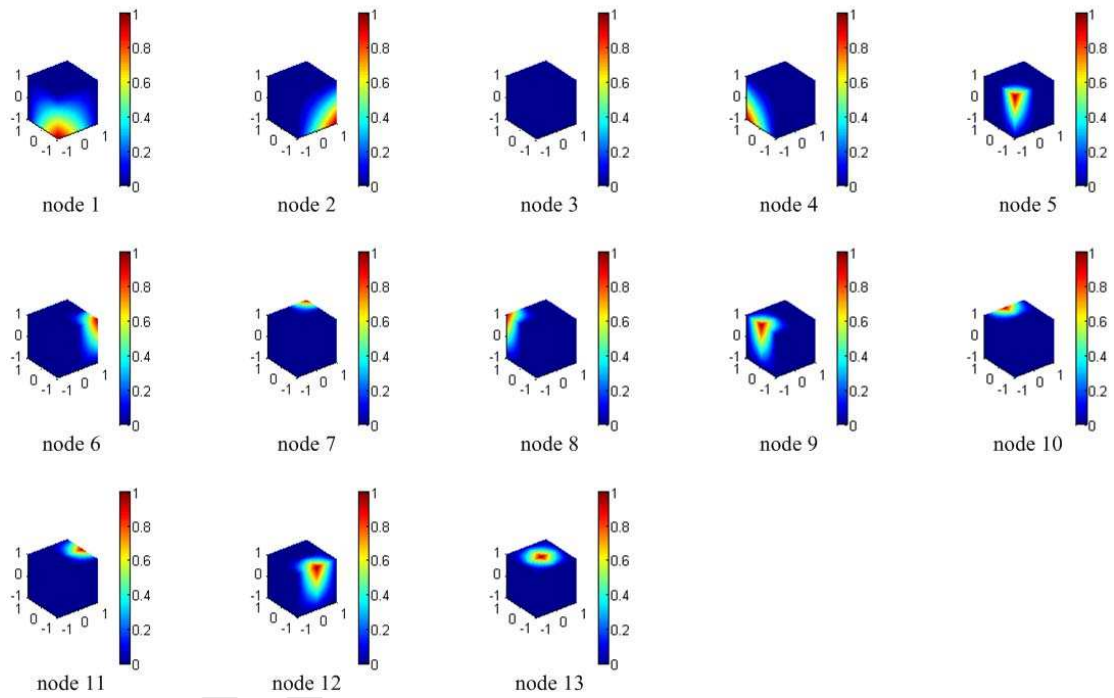


Fig. 2 Schematic notation of a $(8+j+k+l+p+q+r)$ -node element and the definition of its division into seven types of different grouped nodes.



(a)



(b)

Fig. 3 A typical 3-D variable 13-node hexahedron element (a) and its representative shape functions possessing the Kronecker's delta function property at each node.

2.3 Recovery based error estimator

By employing an adaptive refinement procedure, an error estimator must be defined in the model to detect elements that whose determinable relative errors exceed a specific tolerance are refined.

2.3.1 Recovery of the stress fields

In the present work, the recovery of the stress fields can be revised according to the Zienkiewicz–Zhu error estimator [39]. Basically, the enhanced smoothed stresses are recovered by projecting the element stresses onto the nodes, and by interpolating the nodal stresses with the same ansatz functions that are being used for calculating the displacements. In order to accurately reflect stress discontinuity along crack face as well as stress singularity at crack tip, Prange et al. [3] adopted the asymptotic stress fields in linear elastic fracture mechanics as the crack-tip branch enrichment functions for the smoothed stresses. The approximation of smoothed stresses can be written as

$$\sigma^s(x) = \sum_{i \in I} N_i(x) \sigma_i^* + \sum_{j \in J} N_j(x) [H(x) - H(x_j)] a_j^* + \sum_{k \in K} N_k(x) \left\{ \begin{array}{l} \sum_{\alpha=1}^3 [G_{11,\alpha}(x) - G_{11,\alpha}(x_k)] b_{11,k\alpha}^* \\ \sum_{\alpha=1}^3 [G_{22,\alpha}(x) - G_{22,\alpha}(x_k)] b_{22,k\alpha}^* \\ \sum_{\alpha=1}^3 [G_{33,\alpha}(x) - G_{33,\alpha}(x_k)] b_{33,k\alpha}^* \\ \sum_{\alpha=1}^3 [G_{12,\alpha}(x) - G_{12,\alpha}(x_k)] b_{12,k\alpha}^* \\ \sum_{\alpha=1}^3 [G_{13,\alpha}(x) - G_{13,\alpha}(x_k)] b_{13,k\alpha}^* \\ \sum_{\alpha=1}^3 [G_{23,\alpha}(x) - G_{23,\alpha}(x_k)] b_{23,k\alpha}^* \end{array} \right\} \quad (13)$$

where σ_i^* , a_j^* and $b_{pq,k}^*$ reflect the nodal degrees of freedom of the enhanced smoothed stresses.

$G_{pq,\alpha}$ are the crack tip enrichment functions.

For the 3-D isotropic elasticity, the crack-tip enrichment functions $G_{pq,\alpha}$ are defined as [53]

$$G_{11,1} = \frac{1}{\sqrt{r}} \cos\left(\frac{\theta}{2}\right) \left(1 - \sin\left(\frac{\theta}{2}\right) \sin\left(\frac{3\theta}{2}\right)\right) \quad (14a)$$

$$G_{11,2} = \frac{-1}{\sqrt{r}} \sin\left(\frac{\theta}{2}\right) \left(2 + \cos\left(\frac{\theta}{2}\right) \cos\left(\frac{3\theta}{2}\right)\right) \quad (14b)$$

$$G_{11,3} = 0 \quad (14c)$$

$$G_{22,1} = \frac{1}{\sqrt{r}} \cos\left(\frac{\theta}{2}\right) \left(1 + \sin\left(\frac{\theta}{2}\right) \sin\left(\frac{3\theta}{2}\right)\right) \quad (14d)$$

$$G_{22,2} = \frac{1}{\sqrt{r}} \sin\left(\frac{\theta}{2}\right) \cos\left(\frac{\theta}{2}\right) \cos\left(\frac{3\theta}{2}\right) \quad (14e)$$

$$G_{22,3} = 0 \quad (14f)$$

$$G_{12,1} = \frac{1}{\sqrt{r}} \cos\left(\frac{\theta}{2}\right) \sin\left(\frac{\theta}{2}\right) \cos\left(\frac{3\theta}{2}\right) \quad (14g)$$

$$G_{12,2} = \frac{1}{\sqrt{r}} \cos\left(\frac{\theta}{2}\right) \left(1 - \sin\left(\frac{\theta}{2}\right) \sin\left(\frac{3\theta}{2}\right)\right) \quad (14h)$$

$$G_{12,3} = 0 \quad (14i)$$

$$G_{13,1} = G_{13,2} = 0, G_{13,3} = -\frac{1}{\sqrt{r}} \sin\left(\frac{\theta}{2}\right) \quad (14j)$$

$$G_{23,1} = G_{23,2} = 0, G_{23,3} = \frac{1}{\sqrt{r}} \cos\left(\frac{\theta}{2}\right) \quad (14k)$$

$$G_{33,1} = \nu (G_{11,1} + G_{22,1}) \quad (14l)$$

$$G_{33,2} = \nu (G_{11,2} + G_{22,2}) \quad (14m)$$

$$G_{33,3} = \nu (G_{11,3} + G_{22,3}) \quad (14n)$$

where ν is Poisson's ratio.

In order to fully define the smoothed stress field, we need to evaluate the coefficients σ^* , \mathbf{a}^* and \mathbf{b}^* , which is often accomplished by minimization of the square of the L_2 norm of the difference between the XFEM stress field and the smoothed stress field over the whole domain, i.e.,

$$\int_{\Omega} \|\sigma^s - \sigma\|^2 d\Omega \rightarrow \min \quad (15)$$

where $\boldsymbol{\sigma} = [\sigma_x \ \sigma_y \ \sigma_z \ \tau_{xy} \ \tau_{xz} \ \tau_{yz}]$ is the stresses computed by means of the displacement field of the XFEM solution.

From Eq. (15), the following linear equation system can be obtained

$$A\boldsymbol{\chi}^* = \mathbf{B} \quad (16)$$

where $\boldsymbol{\chi}^* = [\boldsymbol{\sigma}^* \ \mathbf{a}^* \ \mathbf{b}^*]^T$ is the vector of nodal unknowns in the smoothed stress field, and A and \mathbf{B} are the coefficient matrix and nodal coefficient vector, respectively.

The element contribution to A is expressed as follows:

$$\mathbf{a}_{ij} = \begin{bmatrix} \mathbf{a}_{ij}^{\sigma^* \sigma^*} & \mathbf{a}_{ij}^{\sigma^* a^*} & \mathbf{a}_{ij}^{\sigma^* b^*} \\ \mathbf{a}_{ij}^{a^* \sigma^*} & \mathbf{a}_{ij}^{a^* a^*} & \mathbf{a}_{ij}^{a^* b^*} \\ \mathbf{a}_{ij}^{b^* \sigma^*} & \mathbf{a}_{ij}^{b^* a^*} & \mathbf{a}_{ij}^{b^* b^*} \end{bmatrix} \quad (17)$$

where

$$\mathbf{a}_{ij}^{rs} = \int_{\Omega_e} (\mathbf{B}_i^r)^T \mathbf{B}_j^s d\Omega; \quad (r, s = \sigma^*, a^*, b^*) \quad (18)$$

with

$$\mathbf{B}_i^{\sigma^*} = \begin{bmatrix} N_i & 0 & 0 & 0 & 0 & 0 \\ 0 & N_i & 0 & 0 & 0 & 0 \\ 0 & 0 & N_i & 0 & 0 & 0 \\ 0 & 0 & 0 & N_i & 0 & 0 \\ 0 & 0 & 0 & 0 & N_i & 0 \\ 0 & 0 & 0 & 0 & 0 & N_i \end{bmatrix} \quad (19)$$

$$\mathbf{B}_i^{a^*} = (H - H_i) \begin{bmatrix} N_i & 0 & 0 & 0 & 0 & 0 \\ 0 & N_i & 0 & 0 & 0 & 0 \\ 0 & 0 & N_i & 0 & 0 & 0 \\ 0 & 0 & 0 & N_i & 0 & 0 \\ 0 & 0 & 0 & 0 & N_i & 0 \\ 0 & 0 & 0 & 0 & 0 & N_i \end{bmatrix} \quad (20)$$

$$\mathbf{B}_i^{b^*} = \begin{bmatrix} \mathbf{B}_{i1}^{b^*} & \mathbf{B}_{i2}^{b^*} & \mathbf{B}_{i3}^{b^*} \end{bmatrix} \quad (21)$$

$$\mathbf{B}_{i1}^{b^*} = N_i \begin{bmatrix} G_{11,1} - G_{11,1}(x_k) & 0 & 0 & 0 & 0 & 0 \\ 0 & G_{22,1} - G_{22,1}(x_k) & 0 & 0 & 0 & 0 \\ 0 & 0 & G_{33,1} - G_{33,1}(x_k) & 0 & 0 & 0 \\ 0 & 0 & 0 & G_{12,1} - G_{12,1}(x_k) & 0 & 0 \\ 0 & 0 & 0 & 0 & G_{13,1} - G_{13,1}(x_k) & 0 \\ 0 & 0 & 0 & 0 & 0 & G_{23,1} - G_{23,1}(x_k) \end{bmatrix} \quad (22)$$

$$\mathbf{B}_{i_2}^{b^*} = N_i \begin{bmatrix} G_{11,2} - G_{11,2}(x_k) & 0 & 0 & 0 & 0 & 0 \\ 0 & G_{22,2} - G_{22,2}(x_k) & 0 & 0 & 0 & 0 \\ 0 & 0 & G_{33,2} - G_{33,2}(x_k) & 0 & 0 & 0 \\ 0 & 0 & 0 & G_{12,2} - G_{12,2}(x_k) & 0 & 0 \\ 0 & 0 & 0 & 0 & G_{13,2} - G_{13,2}(x_k) & 0 \\ 0 & 0 & 0 & 0 & 0 & G_{23,2} - G_{23,2}(x_k) \end{bmatrix} \quad (23)$$

$$\mathbf{B}_{i_3}^{b^*} = N_i \begin{bmatrix} G_{11,3} - G_{11,3}(x_k) & 0 & 0 & 0 & 0 & 0 \\ 0 & G_{22,3} - G_{22,3}(x_k) & 0 & 0 & 0 & 0 \\ 0 & 0 & G_{33,3} - G_{33,3}(x_k) & 0 & 0 & 0 \\ 0 & 0 & 0 & G_{12,3} - G_{12,3}(x_k) & 0 & 0 \\ 0 & 0 & 0 & 0 & G_{13,3} - G_{13,3}(x_k) & 0 \\ 0 & 0 & 0 & 0 & 0 & G_{23,3} - G_{23,3}(x_k) \end{bmatrix} \quad (24)$$

and the element contribution to \mathbf{B} is as follows

$$\mathbf{b}_i = \begin{bmatrix} \mathbf{b}_i^{\sigma^*} & \mathbf{b}_i^{a^*} & \mathbf{b}_i^{b^*} \end{bmatrix} \quad (25)$$

$$\mathbf{b}_i^{\sigma^*} = \int_{\Omega_e} \mathbf{B}_i^{\sigma^*} \sigma d\Omega \quad (26)$$

$$\mathbf{b}_i^{a^*} = \int_{\Omega_e} \mathbf{B}_i^{a^*} \sigma d\Omega \quad (27)$$

$$\mathbf{b}_i^{b^*} = \int_{\Omega_e} \mathbf{B}_i^{b^*} \sigma d\Omega \quad (28)$$

2.3.2 Error estimator

As the error estimator is based on a stress smoothing method, the nodal enhanced stresses are hence recovered with a least square fit. The L_2 norm error of stresses for element i is computed at the element level by the following equation [3]

$$err(i) = \sqrt{\frac{1}{\Omega_e} \int_{\Omega_e} (\boldsymbol{\sigma} - \boldsymbol{\sigma}^s)^T (\boldsymbol{\sigma} - \boldsymbol{\sigma}^s) d\Omega} \quad (29)$$

with Ω_e being the area of the element. The maximum L_2 norm stress of the elements is err_{\max} ,

then the relative discretization error for element i is estimated as

$$\eta(i) = \frac{err(i)}{err_{\max}} \times 100\% \quad (30)$$

This factor is known as an error indicator applicable to subsequently refined meshes, and every element (called parent elements) with a relative discretization error greater than a specified permitted value is refined with a set of sub-elements (called children elements). In this 3-D work, a set of $3 \times 3 \times 3$ sub-division elements or children elements is used throughout the study

unless stated otherwise. One must be noted that this adaptive refinement procedure naturally leads to incompatible hanging nodes between parents and children elements. However, the incompatible feature of the meshes is then merged by the aid of the variable-node transition elements [19, 22].

The L_2 norm error of the stresses for the whole domain is then calculated by

$$err_{\text{Total}} = \sqrt{\int_{\Omega_e} (\boldsymbol{\sigma} - \boldsymbol{\sigma}^s)^T (\boldsymbol{\sigma} - \boldsymbol{\sigma}^s) d\Omega} \quad (31)$$

2.4 Numerical integrations

In the present Lm-XFEM, there exist different types of elements mainly induced by cracks and different scale meshes. The numerical integration used for those elements is crucial and important to the success of the approach. The influence of the numerical integration on the performance and the accuracy of the XFEM in general or the present Lm-XFEM in particular is not trivial. Previous efforts have devoted to the development of effective and accurate methods for the numerical integration in the context of the XFEM. Relevant references are not given here due to the sake of brevity of the manuscript, but interested readers may find them in the literature effortlessly.

To ensure the strain field to be adequately integrated, the following integration schemes are utilized in the present formulation.

(1) *Eight-node hexahedron elements*: For the eight-node hexahedron elements, the conventional second-order Gaussian quadrature scheme is employed for treating elements that do not contain any enriched nodes. For the elements that include enriched nodes (but are not cut by the crack), high-order Gaussian quadrature rule is handled to improve the accuracy of the results. However, it needs a special treatment of the numerical integration for the elements that are cut by a crack or contain a crack-front, called “cut element” and “crack-front element”, respectively. The treatment can be fulfilled by partitioning the cut or split elements and crack-front elements into sub-tetrahedrons, as schematically shown in Fig.4, whose boundaries align with the crack geometry, e.g., see also Refs.[10, 40] for more information. In the sub-tetrahedrons, high-order Gaussian quadrature rules are often taken to ensure and improve the accuracy of the results. Nonetheless, the use of the Gaussian points for all the computations

is detailed in the numerical examples section.

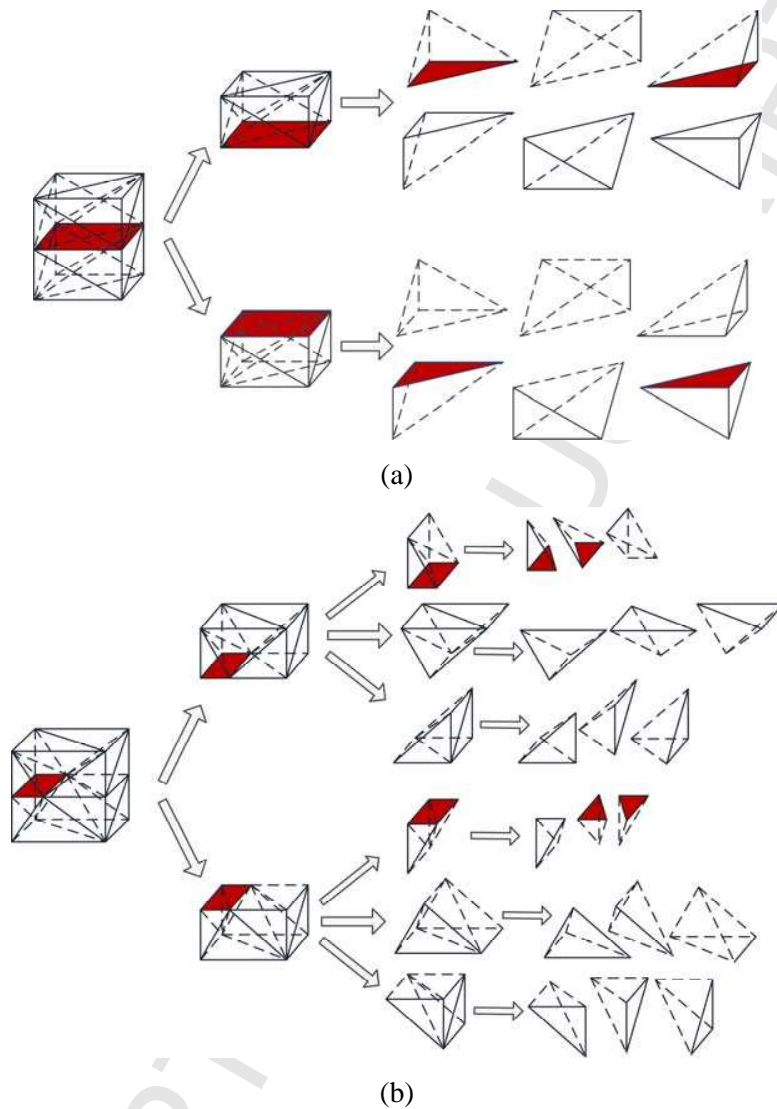


Fig. 4 Generation of sub-tetrahedrons for the quadrature: element cut by a crack (a); and element containing a crack-front (b). The red represents the crack surface.

(2) *Variable-node hexahedron elements*: Since the variable-node elements have been integrated into the model, treating the numerical integration for those variable-node elements that neither contain any crack nor cut by a crack is briefly described here. The nodal shape functions are computed through Eq. (12), and the slope discontinuity of the shape functions may give rise to the inter-subdomain boundaries. To overcome the slope discontinuity in the

numerical integration, sub-hexahedrons are hence generated, where the shape functions still show the linear interpolation within a sub-hexahedron, shown in Fig. 5. The standard second-order Gauss quadrature rule can then be applied for those sub-hexahedrons.

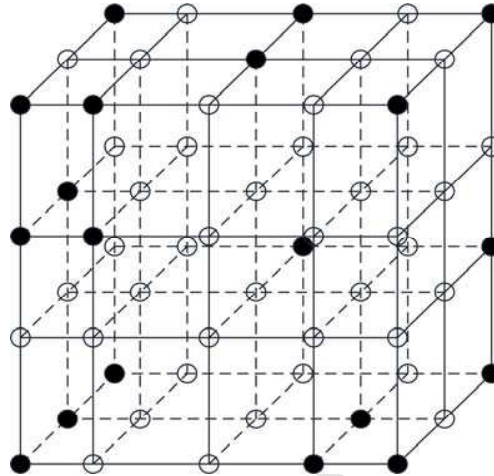


Fig. 5 Generation of quadrature sub-domains for a *regular* variable-node hexahedron element which neither cut by a crack or nor contain a crack. The solid points represent the nodal points, while the hollow points represent the supplementary points.

(3) *Fully cut or split variable-node hexahedron elements*: When the mesh is subsequently refined by more than one step of refinement, the variable-node transition elements may be split by a crack or in other words, a fully cut variable-node element does appear, as a result of representing in Fig. 6. In such circumstance, a special treatment required for the numerical integration of the fully cut variable-node elements is needed. Sub-division of the cut variable-node hexahedron element is performed as schematically depicted in Fig. 7a, and sub-hexahedrons are then obtained. All sub-hexahedrons are denoted by the term “(a)” in the figure, meaning that they are thought as the “cut elements” and their numerical integration is hence treated the same as that for regular cut elements.

(4) *Crack-front variable-node elements*: In some other particular cases, the variable-node transition elements may contain a crack as sketched in Fig. 7b. Although this type of element does not appear to any numerical examples examined in the present manuscript the authors, however, decide to develop it because of the flexibility and applicability of the computer codes.

The treatment of the numerical integration for this case is similar to the previous case of fully cut variable elements, but it is a bit more complicated than the case described in Fig. 7a. For this element, we first bypass or ignore the presence of the crack, sub-hexahedrons are generated at this stage as schematically shown in Fig. 7b. These sub-hexahedrons can then be divided into 3 types. Type 1: elements that are cut by the crack, denoted by the term “(a)” that is the same as in Fig. 7a; Type 2: elements that contain a crack-front, denoted by the term “(b)””; and Type 3: regular elements that neither contain any crack nor cut by crack. Then, the Gauss quadrature scheme is used for the numerical integrations of those types of sub-elements.

Once again, the special treatment of the numerical integration in the present codes as described above is necessary since it is to ensure the convergence of the solutions or avoid some undesirable situations.

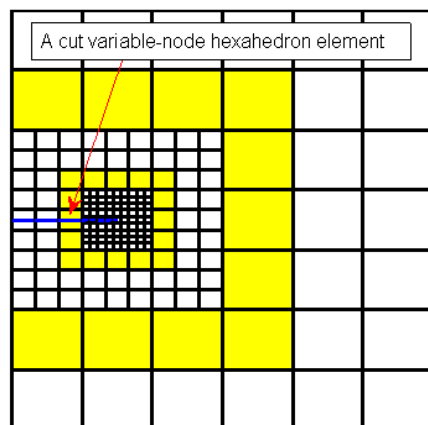


Fig. 6 Hexahedral meshes discretization of a straight edge crack in a finite 3-D solid obtained by two steps of refinement. A fully cut variable-node hexahedron element appears in the model when the mesh is refined up to the second step of refinement. The larger layer of variable-node transition elements as marked in yellow obtained by the first step of refinement, while the smaller layer, also marked in yellow, is gained by the subsequent second step. It is obvious to see a fully cut variable-node hexahedron element appeared therein. The blue line represents the crack.

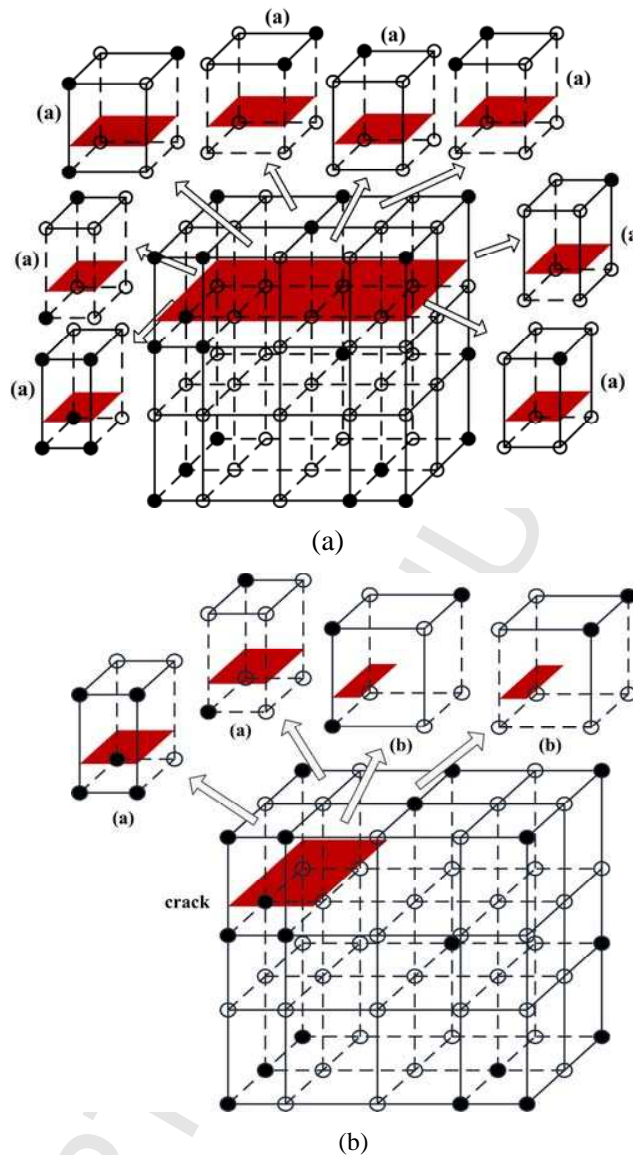


Fig. 7 Generation of quadrature sub-domains for a variable-node hexahedron element: A fully cut variable-node hexahedron element (a); and a crack-front variable-node hexahedron element (b). The solid points represent the nodal points, while the hollow points represent the supplementary points. The crack surface is marked and filled in red.

2.5 Numerical implementation

Before closing this section, let us summarize the main solution procedure of the whole problem by using the proposed method:

- (1) The problem domain is discretized with coarse-scale meshes, without considering the crack shape and location.
- (2) Loop over the number of refinement.
 - a. Enriched nodes are selected using the level set method.
 - b. Assemble the global stiffness matrix and load array.
 - c. Solve the governing equations considering the constraint conditions.
 - d. Calculate the smoothed stress field through Eq. (13).
 - e. Calculate the L2 norm error of the stresses for each element through Eq. (29).
 - f. Calculate the relative error for each element through Eq. (30).
 - g. The elements in which the relative error exceeds the tolerance are refined.
- (3) Evaluate the stress intensity factors.

3. Stress intensity factors computation

In linear elastic fracture mechanics for solids, the stress intensity factors (SIFs) are the most important characterizing fracture parameters to represent the strength of the singular fields at the crack tips. The SIFs can be obtained based on the results from three-dimensional local mesh refinement XFEM. Several previous methods have been proposed to determine the SIFs, such as the displacement extrapolation method near the crack tip [41], the virtual crack extension method [49], the virtual crack closure method [50], and the M-integral method [51]. Though the M-integral method has found to be one of the best methods for two-dimension problems, the accurate determination of the SIFs based on the M-integral method, especially for three-dimensional curved crack, is related to the integration path issue, and the relationship between them has not been well interpreted yet. González-Albuixech et al. [52] pointed out that the domain extraction is controlled through the use of a specific function dependent upon the level set coordinates, while Moës et al. [42] took the domain as a parallelepiped one. The displacement extrapolation method can be used for direct evaluation of the SIFs according to

the relative crack surface displacements. Throughout this study, the displacement extrapolation method is employed for estimating the SIFs for our 3-D numerical examples.

Nevertheless, future works would be interesting if the M_1 -integral method could be integrated into the present formulation to extract the fracture parameters. In fact the authors have made some preliminary attempts to the use of the M_1 -integral method for extracting the SIFs of planar 3-D straight and curved cracks in the framework of the Lm-XFEM. The accuracy that we have observed however does not reach our final goal as less accuracy is observed in the SIFs exacted by the method for 3-D curved cracks, and more importantly the dependent path of J-integral is problematic. Further developments to improve the accuracy of the SIFs using the M_1 -integral method for 3-D curved cracks are thus necessary, but it would probably take much effort in fulfilling the tasks, and in the present circumstance it is out of the scope of this manuscript. Therefore, we have scheduled to study this discussed issue in our next manuscript comprehensively.

In the crack-tip Cartesian coordinates, the relation between the relative displacements and the SIFs are [54]

$$K_I = \frac{\sqrt{2\pi G}}{(1+k)\sqrt{r}} |\Delta v| \quad (32)$$

$$K_{II} = \frac{\sqrt{2\pi G}}{(1+k)\sqrt{r}} |\Delta u| \quad (33)$$

$$K_{III} = \frac{\sqrt{2\pi G}}{(1+k)\sqrt{r}} |\Delta w| \quad (34)$$

where G is the shearing modulus; $k = \frac{3-\nu}{1+\nu}$, ν is the Poisson's ratio; r is the ray distance from the crack front; while $|\Delta u|$, $|\Delta v|$, and $|\Delta w|$ are the relative displacements near the crack front in the crack front Cartesian coordinates on the crack surface.

Some points in the same normal direction from the crack front on the crack surface is taken to construct a set array $(r_i, K_{Ii}, K_{IIi}, K_{IIIi})$, where r_i is the distance from point i to the crack front and K_{Ii} , K_{IIi} , K_{IIIi} are the SIFs of point i . By using the least squares method to fit the set array, the SIFs at crack front can then be determined through the following relations [55]:

$$K_I \approx \frac{\sum r_i \sum r_i K_{Ii} - \sum r_i^2 \sum K_{Ii}}{(\sum r_i)^2 - N \sum r_i^2} \quad (35a)$$

$$K_{II} \approx \frac{\sum r_i \sum r_i K_{IIi} - \sum r_i^2 \sum K_{IIi}}{(\sum r_i)^2 - N \sum r_i^2} \quad (35b)$$

$$K_{III} \approx \frac{\sum r_i \sum r_i K_{IIIi} - \sum r_i^2 \sum K_{IIIi}}{(\sum r_i)^2 - N \sum r_i^2} \quad (35c)$$

where N is the number of chosen points in the same normal direction from the crack front on the crack surface, $N = 10$ is adopted in this study.

From Eq. (1), it is obvious that the relative displacements on the crack surface depend only on the enrichment variables, so it is easy to determine the SIFs using the relative displacements on the crack surface in the XFEM.

4. Numerical experiments and discussions

In this section, we particularly concentrate our attention on numerical experiments and accurate investigation of the SIFs calculated by the present method. An in-house 3-D MATLAB code for solving SIFs using the 3-D local mesh refinement XFEM with variable-node hexahedron elements is developed. To this end, six numerical examples of planar straight and curved cracks embedded in 3-D solids with single and mixed-mode fractures are hence considered:

- The first three examples deal with single and mixed-mode fracture in 3-D by considering an edge straight crack, a central straight crack and an edge inclined straight crack.
- The last three examples deal with curved cracks in 3-D by considering a central penny shaped crack, a central ellipse shaped crack and an edge ellipse shaped crack.

All the numerical results are analyzed and validated against the reference solutions to show the accuracy and effectiveness of the developed Lm-XFEM. The SIFs extracted by using the displacement extrapolation method are then compared with analytical solutions available in literature and the conventional XFEM with fine meshes.

Regarding the number of Gaussian quadrature point used in the numerical computations, the cut or split element is divided into 12 sub-elements and each sub-element uses 4 Gaussian points, so all of them total 48 points. For the tip element, it is divided into 18 sub-elements and each of them uses 5 Gaussian points and thus its total is 90 points. Elements that do not contain any crack but engage tip nodes use $4 \times 4 \times 4$ Gaussian points, while other elements use $2 \times 2 \times 2$ points.

4.1 An edge straight crack

A cube of size $10\text{m} \times 10\text{m} \times 10\text{m}$ containing an edge straight crack as schematically depicted in Fig. 8 is considered. A crack length of 2.5m as shown in the figure is taken. The top surface of the cube is subjected to a uniform traction of $\sigma = 1\text{Pa}$ while the bottom surface is constrained in all directions. The following material parameters, the Young's modulus $E = 206\text{GPa}$ and the Poisson ratio $\nu = 0.3$, are used throughout the study if not specified otherwise.

Under the plane strain condition, the analytical solution of this edge crack problem for $\frac{d}{l} \leq 0.6$ is given by [56]

$$K_I^{\text{ref}} = \sigma \sqrt{\pi d} F \left(\frac{d}{l} \right) \quad (36)$$

with

$$F = 1.12 - 0.231 \frac{d}{l} + 10.55 \left(\frac{d}{l} \right)^2 - 21.72 \left(\frac{d}{l} \right)^3 + 30.39 \left(\frac{d}{l} \right)^4 \quad (37)$$

where d denotes the crack length while l is the length of the cube along the crack direction.

For this example, only mode-I SIF is extracted using the displacement extrapolation method. The mode-I SIF is then estimated for each step of refinement using the Lm-XFEM and is compared with the results derived from the conventional XFEM as well as analytical solutions. The study is to show the accuracy of the developed Lm-XFEM in determining the SIFs of a planar 3-D edge straight crack in a elastic cube.

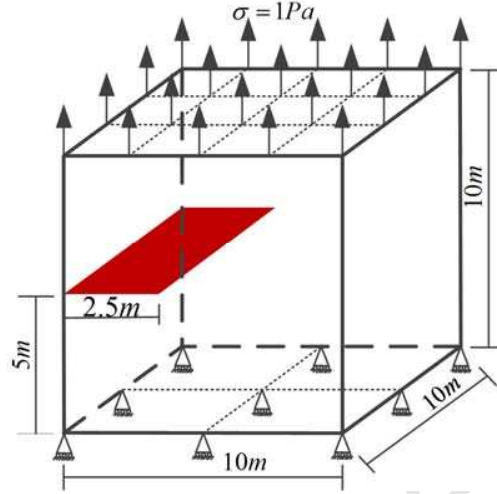


Fig. 8 Geometric notation of a cube with an edge straight crack (in red) and its configuration parameters

A tolerance error of 0.1 is taken for this example. By applying the proposed procedure, the elements which have a relative error greater than the specific tolerance error will be refined with $3 \times 3 \times 3$ sub-elements. It means that an eight-node hexahedron element (say *parent element*), which has been detected to be refined, is then sub-divided into $3 \times 3 \times 3$ sub-elements (say *children elements*). Actually, the children elements can be arbitrary, but based on our numerical experiments, refinement with a set of $3 \times 3 \times 3$ children elements is recommended and we use this set throughout the study unless stated otherwise.

An initial mesh, $7 \times 7 \times 7$ elements as shown in Fig. 9a for instance, is generated using the Lm-XFEM as its initial step of refinement. The adaptive algorithm based on error estimator is then applied and all the discretized elements of the domain of interest are detected and a set of elements around the crack is selected and labeled. The detected elements are those that will be refined in the next step of refinement algorithm. As a result, the initial mesh in Fig. 9a is then refined that results in a refined mesh as depicted in Fig. 9b. The algorithm is repeated the same for the next refinement until reaching the specified number of steps. Fig. 9c shows the mesh fulfilled by the second step of refinement. Interestingly, it can be observed in Fig. 9c that the refined mesh discretized by the second step of refinement contains a variable-node transition element cut by crack. That is exactly the case that we have discussed and can be found in the

numerical integration, i.e., subsection 2.4.

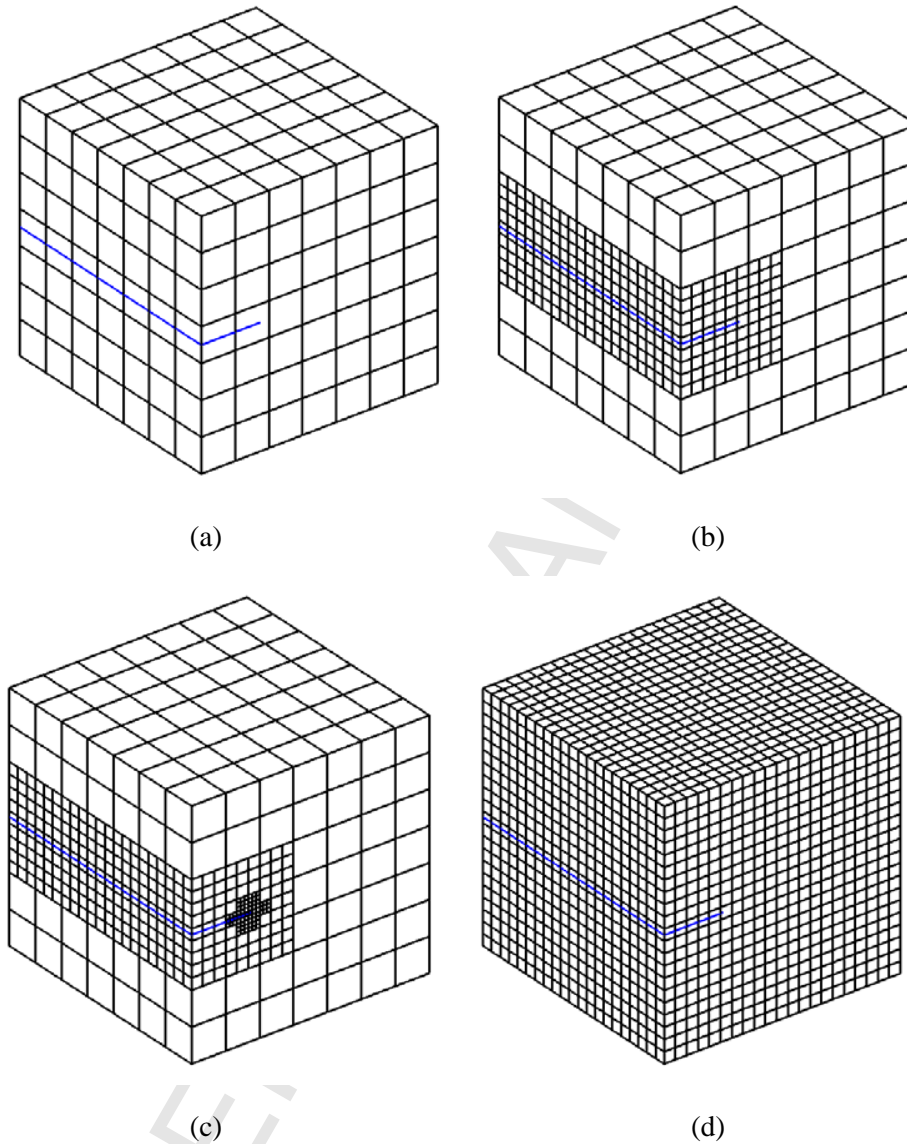


Fig. 9 An edge straight crack in a finite domain: initial mesh (a); the first refined Lm-XFEM mesh (b); the second refined Lm-XFEM mesh (c) and a mesh using the conventional XFEM (d)

It is important to stress here that the number of refinement steps must be defined by the analysts. Our own numerical experiments particularly in this work have found that by indicating one or two steps of refinement acceptable solutions could be reached. For practical

purposes however at least two steps of refinement or even more is recommended. Determining an appropriate number of refinement steps for each particular problem is trivial.

The subsequent numerical investigations, one or two steps of refinement have been examined and studied. For comparison, the entire computational domain using small-scale elements as shown in Fig. 9d is also added, which is derived from the conventional XFEM. All the meshes sketched in Fig. 9 are very interesting since it reveals the advantages of the developed Lm-XFEM over the traditional XFEM. It is because the refined mesh deals with the region that only covers the crack and the areas far from the crack do not take into account. In addition, the number of elements or nodes gained by the conventional XFEM is much larger than that discretized by the Lm-XFEM. This issue is addressed and illustrated in the following numerical results.

For convenience in representing the numerical results, the SIFs are normalized by $K_I^* = K_I / \sigma \sqrt{\pi d}$. Fig. 10 shows the calculated results of K_I^* at crack front with respect to different distances along crack front using the Lm-XFEM and the conventional XFEM with a fine mesh, e.g., $21 \times 21 \times 21$ elements. Unlike the edge crack in 2-D solids where only one crack tip exists, the edge crack in 3-D is however more complicated than that as there exists a crack front (not a crack tip). The K_I^* at certain points at the crack front, different locations, are computed and presented here. Therefore, the numerical results plotted in Fig. 10 represent the K_I^* at different distances along the crack front. The K_I^* results gained by the Lm-XFEM approach well to the exact solutions. Not surprisingly, the initial results using the initial mesh exhibit so poor but the accuracy of the K_I^* increases significantly after each step of refinement, which exactly reflects the desirable characteristics of the developed Lm-XFEM. In addition, the accuracy of the SIFs calculated by the standard XFEM with a fine mesh is far way from the exact solutions as compared with that derived from the second step of refinement using the Lm-XFEM. From the results sketched in Fig. 10, one can see that the SIFs measured at different locations along the crack front are slightly different.

There is another interesting point regarding the standard XFEM that must be discussed here. It is, in general, the accuracy of the standard XFEM can be further improved by taking a finer

mesh, but one must pay attention to the considerable computational time of the conventional XFEM if a very fine mesh is taken. In practices, the efficiency of a method must be taken into account and the refinement methods, often, like the one being studied in this work, is preferable. Nevertheless, the number of elements discretized by using the Lm-XFEM is much less than that by the common XFEM. This feature is one of the advantages of the Lm-XFEM, and that makes the method to be an ideal candidate for practical problems. Furthermore, Table 1 presents the SIFs results computed by the Lm-XFEM and the common XFEM at the central point of the crack front. The numerical results in Table 1 are very interesting as the number of DOFs and the percentage errors reported reveal the domination of the present method. Clearly, it is important to see that high accuracy can be achieved through the Lm-XFEM but a much less number of DOFs compared to the conventional XFEM is used. The adaptive refinement significantly improves the accuracy as it can be clearly seen in Table 1 (or Fig. 10) for the first and second steps of the refinements. Consequently, by employing the Lm-XFEM, we not only obtain high accuracy on the SIFs, but the computational time can also be saved. From Table 1, it is found that the accuracy of the SIFs from the displacement extrapolation method near the crack tip is slightly lower than that from the M-integral method [51].

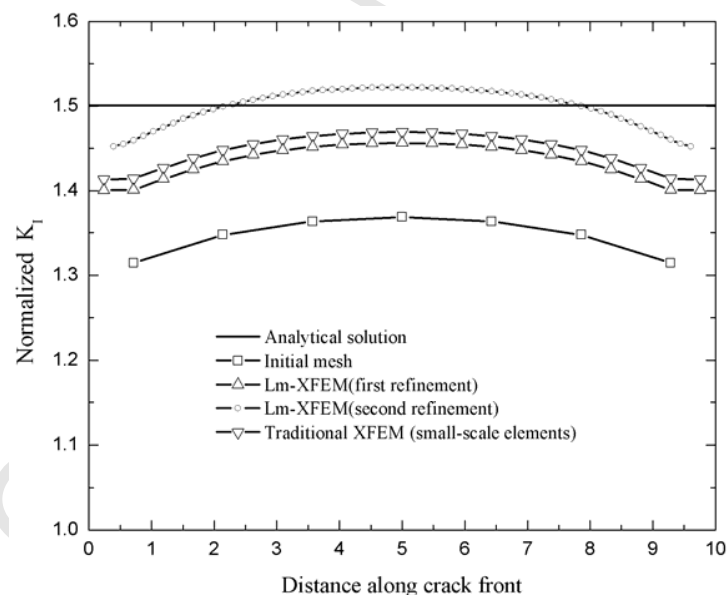


Fig. 10 Comparison of the normalized stress intensity factor (mode-I) at different distance along the crack front for a cube with an edge straight crack among the Lm-XFEM, the conventional XFEM and the exact solution.

Table 1

Normalized stress intensity factor (mode-I) and its percentage errors obtained by the Lm-XFEM for different steps of refinements of an edge straight crack at the central point of crack front. The exact solutions and the conventional XFEM results are also added for the comparison purpose. The values in the () are obtained with the M-integral method [51].

	Exact	Initial mesh	First refined	Second refined	XFEM
DOFs		512	2548	8248	10648
K_I^*	1.5010	1.36867(1.4040)	1.45631(1.5418)	1.52191(1.5205)	1.46919(1.5323)
Error (%)		-8.8137(-6.4694)	-2.9748(2.7204)	1.3958(1.2987)	-2.1166(2.0877)

A specified tolerance error has been used in all the computations but remarks on its selection are addressed here. Theoretically, the smaller the tolerance is taken the better the results are obtained. However, the computational cost must be a critical factor for the selection of this tolerance error. The tolerance error for a given problem can be straightforwardly determined through numerical experiments using the Lm-XFEM as the accuracy is controlled due to the adaptive algorithm. We have found that different problems may use different values of tolerance error, but its determination is trivial. Throughout the study, a tolerance error of 0.1 is taken.

4.2. A central straight crack

The same cube as the previous example, which has a size of $10\text{m} \times 10\text{m} \times 10\text{m}$ containing a central straight crack as schematically depicted in Fig. 11, is considered. The boundary condition applied to the bottom surface and the loading applied to the top surface of cube are assumed the same as the previous example. A crack length of 2m is taken. Under the plane strain condition, the analytical solution of this central crack problem is determined by $K_I = p\sqrt{\pi a}$ [53], where a is half of the center crack length.

Fig. 12a shows an initial mesh of $9 \times 9 \times 9$ elements and its refined mesh for the first step of refinement is shown in Fig. 12b. The figure representing the refined mesh indicates clearly that

only region around the crack is refined, and this is a great advantage of the method, especially for 3-D problems where the computational efficiency takes place as a critical factor.

The SIFs are calculated using the displacement extrapolation method for only one crack front due to the symmetric configuration. The computed SIFs at different distance along the crack front for the central crack are visualized in Fig. 13, showing a comparison between the present results with respect to the conventional XFEM solution using a fine mesh of $27 \times 27 \times 27$ elements. Note that the SIFs reported here represent their real values and are not normalized. The SIFs based on the initial mesh is again found to be inaccurate whereas that achieved by the Lm-XFEM approach well to the exact solutions [53] and match well with the common XFEM results. We perform only one step of refinement since its results obtained are adequately accurate, and further steps of refinement may not be necessary. However, as stated above higher numbers of refinement steps may be necessary, especially for practical problems.

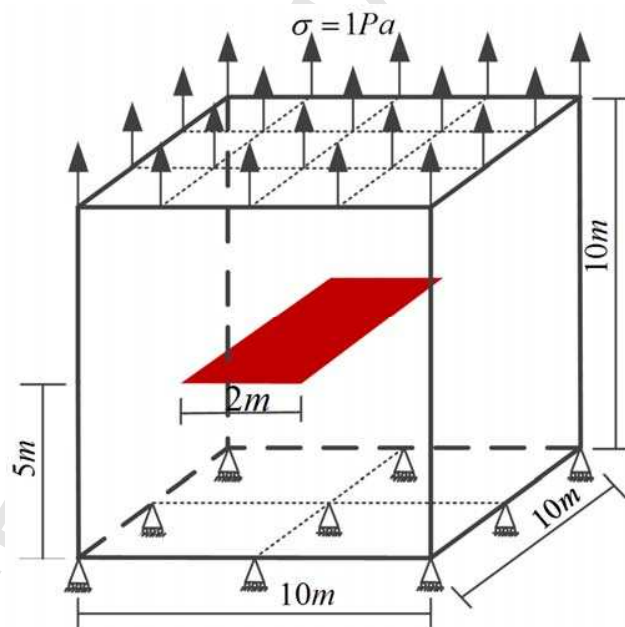


Fig. 11 Geometric notation of a cube with a central straight crack and its configuration parameters showing the boundary and loading conditions

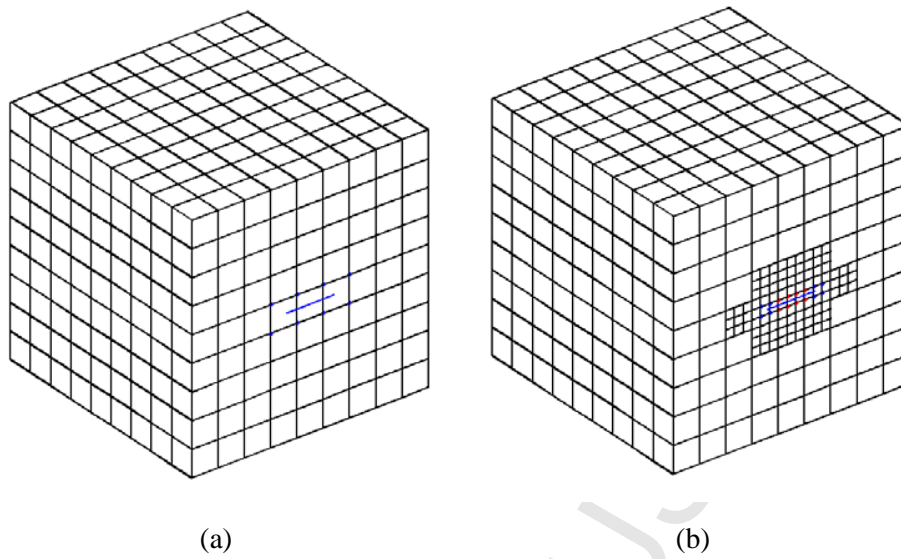


Fig. 12 A central straight crack in a finite domain: Initial mesh (a); and $3 \times 3 \times 3$ refined Lm-XFEM mesh (b).

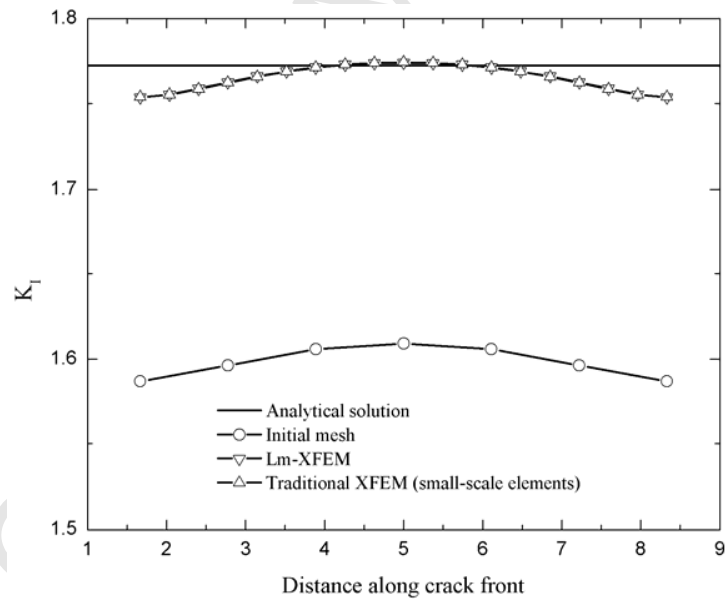


Fig. 13 Comparison of the stress intensity factor (mode-I) at different distance along the crack front for a cube with a central straight crack among the Lm-XFEM, the traditional XFEM and the exact solution.

4.3. A mixed-mode edge inclined straight crack

This example is mainly devoted to study the mixed-mode fracture problem in 3-D planar cracks using the present method. It is accomplished by considering an edge inclined straight crack in a plate under uniform tension as depicted in Fig.14. The size of the plate is $10\text{m} \times 25\text{m} \times 25\text{m}$ and the angle of the inclined crack is set to be 45° . The material parameters and the boundary conditions as well as the loading conditions are taken the same as the previous examples. The length of the crack front is equal to the size of the body, i.e., 25m, see Fig. 14, while the crack length is indicated by a as shown in the same figure. Different crack lengths are studied by varying a from 3 to 5, and the corresponding SIFs for each a are then estimated, respectively.

In this example, two different sets of subdivisions elements or children elements e. g., $2 \times 2 \times 2$ and $3 \times 3 \times 3$, are considered. The use of different sets of subdivided elements is to clarify the effect of the number of subdivisions per element on the accuracy of the SIFs. The same initial mesh of $5 \times 11 \times 11$ elements as sketched in Fig. 15a is taken, and the refined meshes derived from the Lm-XFEM for the two subdivisions of $2 \times 2 \times 2$ and $3 \times 3 \times 3$ children elements are shown in Figs. 15b and 15c, respectively. Note that the refined meshes for $a = 3\text{m}$, for instance, is performed. The SIFs are calculated by the displacement extrapolation method with one step of refinement for different values of the parameter a . They are then normalized by $K_{I,II}^* = K_{I,II} / \sigma \sqrt{\pi d}$ and eventually depicted in Figs. 16a (mode-I) and 16b (mode-II), respectively. The normalized mode-I and mode-II are estimated at a central position of the crack front. Numerical results for each set of subdivided children elements are calculated for different values of a . Compared with the reference solutions given by Institute of China Aeronaut [57], the Lm-XFEM using the subdivided set of $3 \times 3 \times 3$ children elements offers the $K_{I,II}^*$ more accurate than that utilizing the subdivided set of $2 \times 2 \times 2$ elements. In other words, the SIFs derived from the $3 \times 3 \times 3$ children elements approach to the exact solutions better than that from $2 \times 2 \times 2$ elements. More interestingly, it is very important to note that the effect of the crack length on the $K_{I,II}^*$ is significant. The $K_{I,II}^*$ SIFs increase with increasing the crack length,

as a result of the finite size effect in fracture mechanic problems.

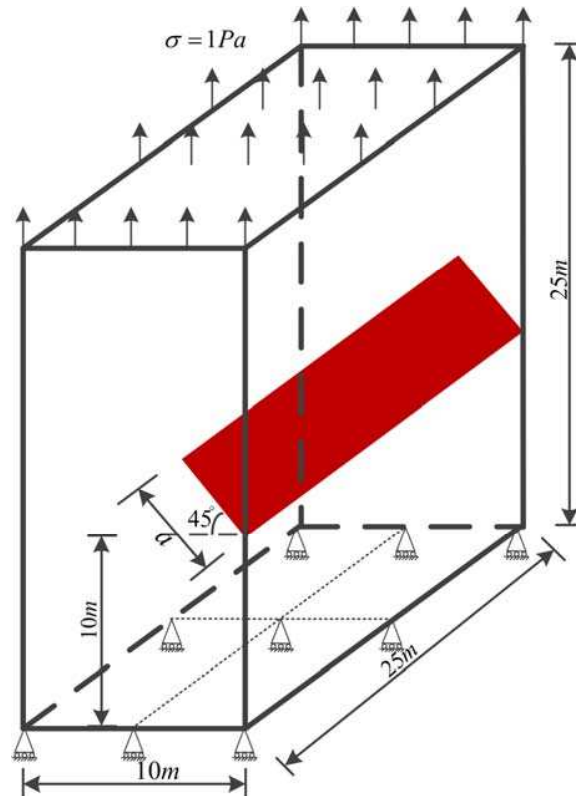


Fig. 14 Schematic configuration of an edge inclined straight crack in a finite domain showing the boundary and loading conditions

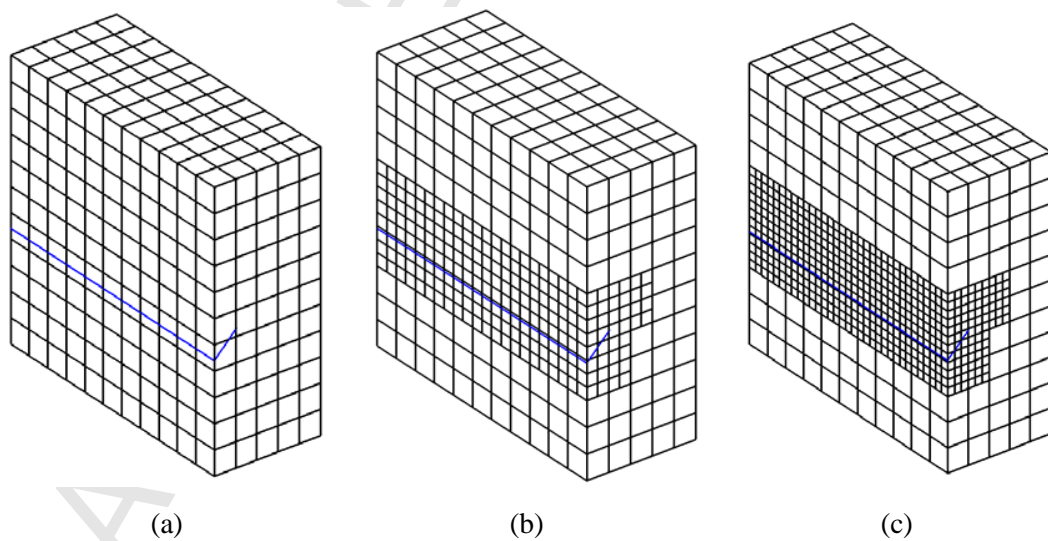


Fig. 15 An edge inclined crack in a finite domain for a crack-length of $a = 3\text{m}$: Initial mesh (a);

a $2 \times 2 \times 2$ refined Lm-XFEM mesh (b) and a $3 \times 3 \times 3$ refined Lm-XFEM mesh (c).

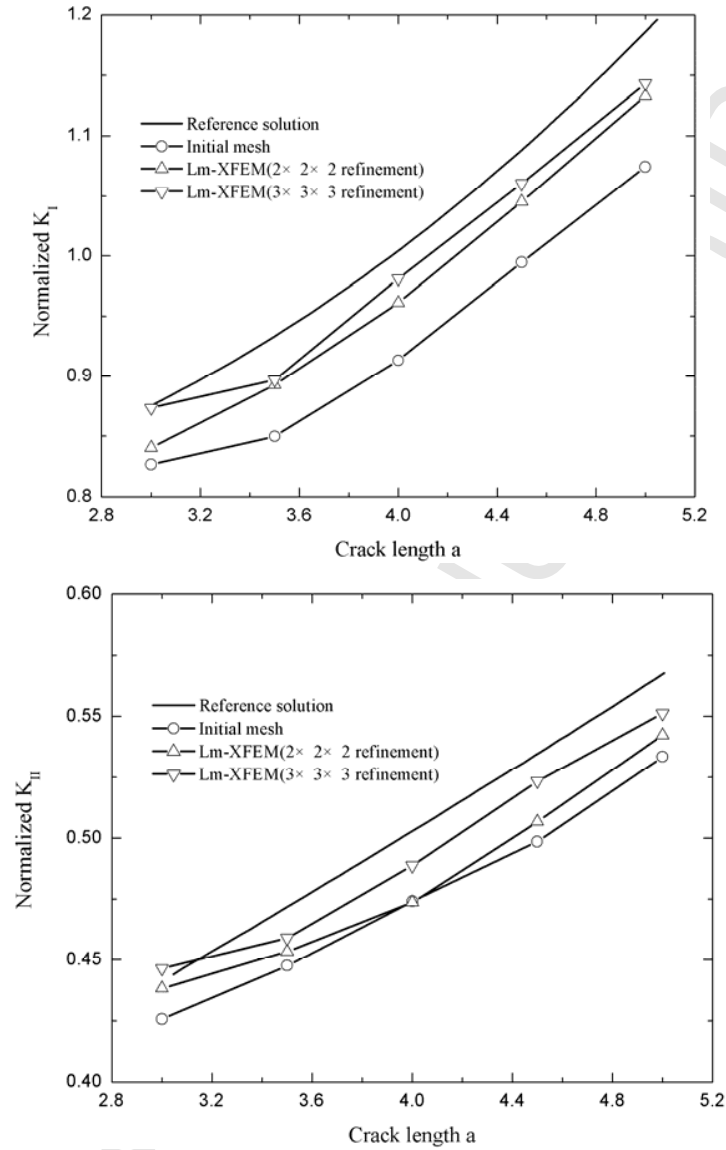


Fig. 16 Variation of the normalized stress intensity factors $K_{I,II}^*$ with respect to crack length a .

4.4. A central penny shaped crack

Accurate numerical simulation of planar curved cracks in 3-D is difficult and remains a challenging problem in the computational mechanics. Specially, accurately determining the SIFs of 3-D curved cracks is still an important topic as many preceding efforts have put onto the improvement of the accuracy of the solutions. In this study, the three following examples are

devoted to illustrate the applicability of the developed Lm-XFEM in simulating 3-D curved cracks. The accuracy of the SIFs are hence examined and validated.

We start by examining a cuboid of size $1\text{m} \times 1\text{m} \times 1\text{m}$ containing a penny shaped crack as shown in Fig.17. The radius of the penny is taken as $r = 0.1\text{m}$. The analytical solutions of this

problem are available in Ref. [58], i.e., $K_{\text{I}} = 2\sigma\sqrt{\frac{r}{\pi}}$ and $K_{\text{II}} = K_{\text{III}} = 0$. Similarly, the

Lm-XFEM is applied to solve this example. By accomplishing that, an initial mesh of $9 \times 9 \times 9$ elements is discretized using the Lm-XFEM. Fig. 18a shows the top-side view of cross-section for the initial mesh of the penny shaped crack while its refined mesh is sketched in Fig. 18b, also the top-side view of cross-section. Different from the previous examples, the SIFs for this penny shaped crack are however estimated at different angles and their computed results are plotted in Fig. 19. Note that the SIFs reported here represent their real values and are not normalized. For verification, results obtained by the traditional XFEM with a fine mesh are also added. The present results indicate the accuracy of the Lm-XFEM as its obtained SIFs approach well to the exact solutions. The SIFs obtained by the traditional XFEM using a fine mesh of $27 \times 27 \times 27$ elements are in a good agreement with the Lm-XFEM as clearly shown in the figure. Even through the accuracy of the SIFs is equivalent but one must note that the great difference distinguishing between the Lm-XFEM and the traditional XFEM is the computational cost and the number of DOFs that are being used for the implementation. The Lm-XFEM with refinement and adaptive algorithm always offers a great advantage over the traditional XFEM to these facts. Nonetheless, the SIFs of this penny shaped crack behave an oscillation around the exact solutions for some angles at the crack front. However, the error on the numerical results obtained by the Lm-XFEM with respect to the exact solutions is small. It is noted that the “bump” of the SIFs obtained by the XFEM in Fig. 19 can be caused by the finite domain used in the computations. By increasing the computational domain the error can substantially be reduced.

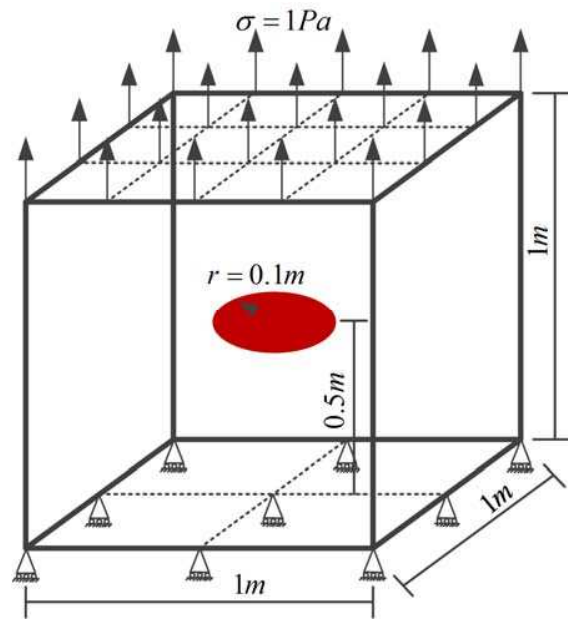


Fig. 17 Schematic configuration of a central penny shaped crack in a finite domain showing the boundary and loading conditions

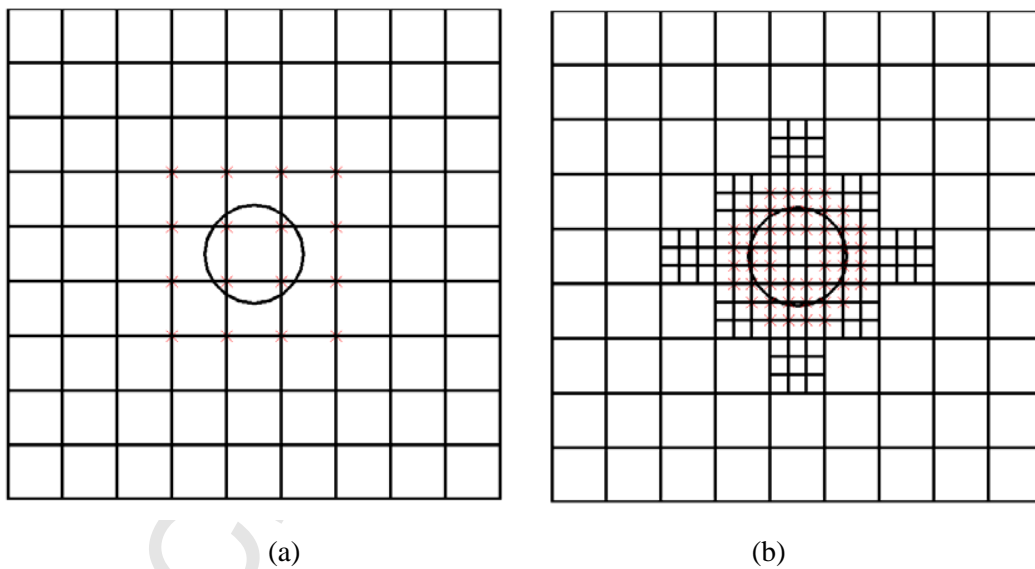


Fig.18 Top-side views of cross-section of a central penny shaped crack in a finite domain: initial mesh (a); a $3 \times 3 \times 3$ refined Lm-XFEM mesh (b)

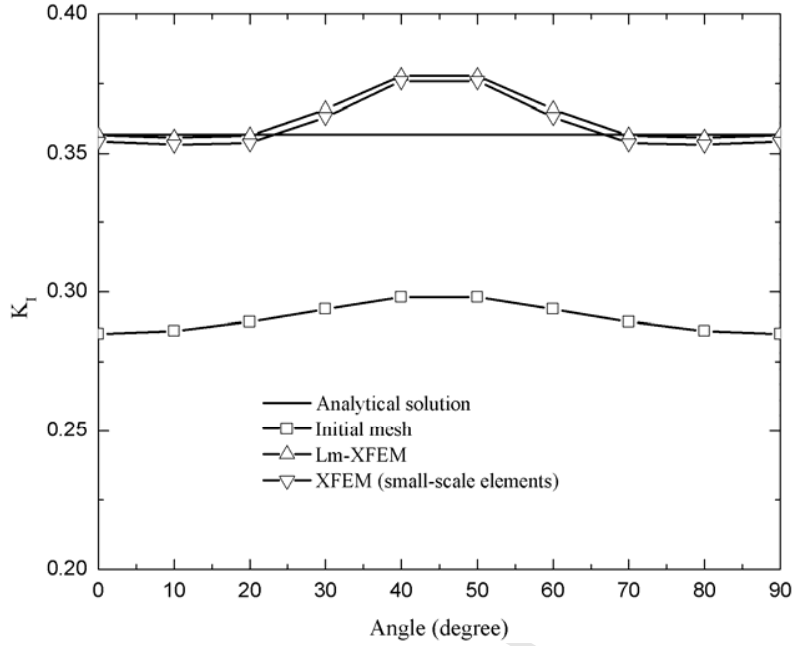


Fig. 19 Comparison of the stress intensity factor (mode-I) at different angles of crack front for a cuboid with a central penny shaped crack among the Lm-XFEM, the conventional XFEM and the exact solution.

4.5. A central ellipse shaped crack

Similar to the penny shaped crack, this example deals with a cuboid of size $1\text{m} \times 1\text{m} \times 1\text{m}$ but contains a central ellipse shaped crack as schematically shown in Fig. 20. We consider the elliptical crack with semi-major axis $a = 0.1\text{m}$ and semi-minor axis $b = 0.05\text{m}$. Since the crack dimensions are small compared to the specimen, we use the infinite domain solution as the reference solution. The exact SIFs solution for a planar central elliptical crack in an infinite domain is given by Irwin [59] and Sukumar et al. [40]

$$K_I = \frac{\sigma\sqrt{\pi b}}{E(k)} \left\{ \sin^2 \theta + \frac{b^2}{a^2} \cos^2 \theta \right\}^{1/4} \quad (38)$$

where θ is the elliptic angle as depicted in Fig. 21, which is to show the position of the crack front, and $E(k)$ is the elliptic integral of the second type and is given by

$$E(k) = \int_0^{\pi/2} \sqrt{1 - k^2 \sin^2 \theta} d\theta; \quad k^2 = \frac{a^2 - b^2}{a^2} \quad (39)$$

The Lm-XFEM is employed to solve the central ellipse shaped crack example and the SIFs estimated with the aid of the displacement extrapolation method are hence visualized in Fig. 22. Note again that the SIFs presented here are their real values and not normalized. Once again, the agreement between the present results using the Lm-XFEM with refined mesh and the exact solutions is good. The difference on the two solutions is small and acceptable, but the maximum error in the SIFs is observed at $\theta = 0^\circ$.

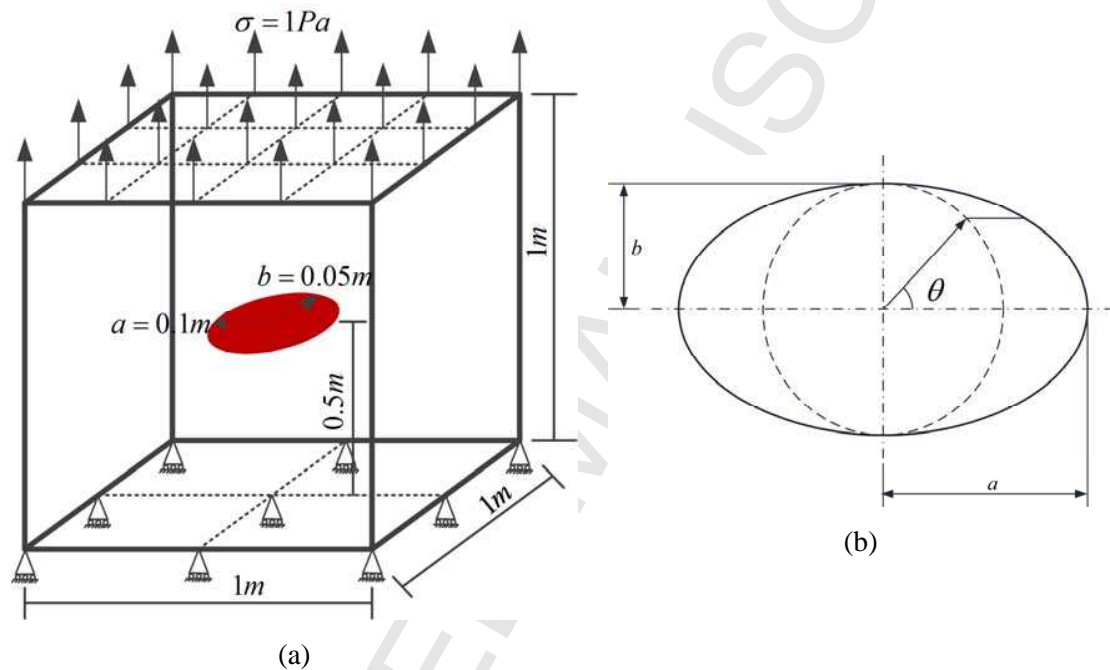


Fig. 20 Schematic configuration of a central ellipse crack in a finite domain showing the boundary and loading conditions (a); and close-up of crack and angle (b).

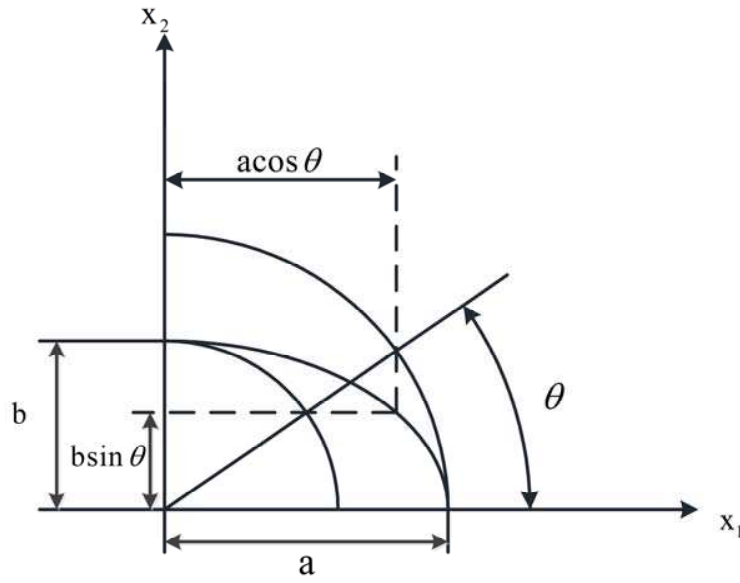


Fig. 21 Geometric definitions for a central ellipse shaped crack

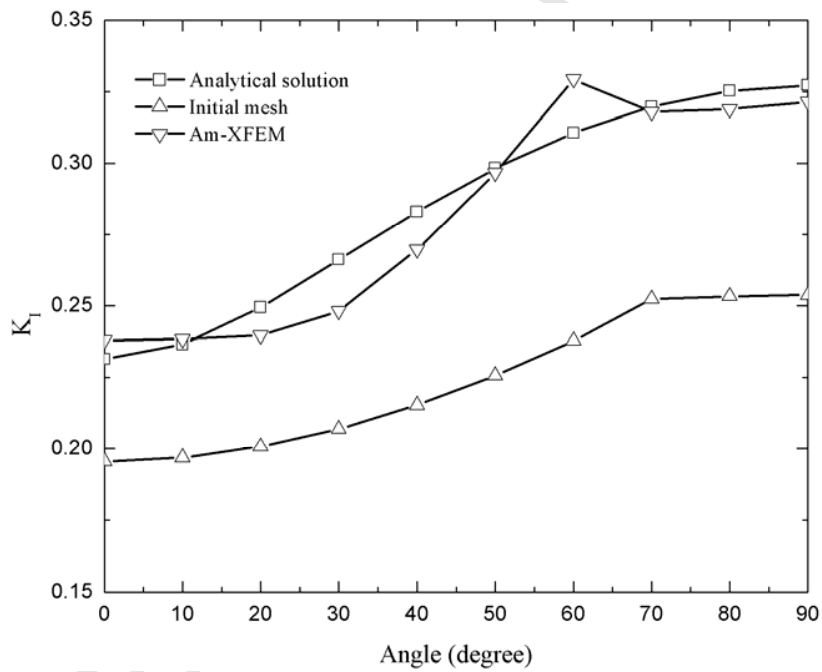


Fig. 22 Mode-I stress intensity factor at different angles of crack front for a cuboid with a central ellipse shaped crack obtained by the Lm-XFEM.

4.6. An edge ellipse shaped crack

Last example deals with an edge ellipse shaped crack in a plate under uniform tension as shown as Fig. 23. The size of the plate is set to be $10\text{m} \times 4\text{m} \times 10\text{m}$ and the elliptical crack's semi-major axis $c = 2\text{m}$ and semi-minor axis $a = 1\text{m}$. The body is also subjected to a uniform traction of $\sigma = 1Pa$ and the bottom surface is also constrained in all the direction. This problem has been analyzed previously by different methods and numerical solutions are readily available in the literature. Among the solutions available, the one derived from Newman and Raju [60] is widely used. The stress intensity factors are normalized by

$$K_I^* = K_I / \sigma \sqrt{\frac{\pi a}{Q}} ac \quad (40)$$

with

$$Q = \begin{cases} 1 + 1.464(a/c)^{1.65} & \text{if } (a/c) \leq 1 \\ 1 + 1.464(c/a)^{1.65} & \text{if } (c/a) > 1 \end{cases} \quad (41)$$

We use a set of initial mesh of $5 \times 11 \times 11$ elements to this example. To show the effect of the number of subdivision elements of children elements on the SIFs, we hence consider two different sets of the number of subdivision, for instance, $3 \times 3 \times 3$ and $5 \times 5 \times 5$. Fig. 24a sketches the initial mesh of edge ellipse shaped crack. Note that the top-side view of cross-section is shown due to the convenience in the representation of the 3-D crack. Figs. 24b and 24c, respectively, depict the refined meshes of the cracks using the suggested number of subdivision elements discretized by the adaptive refinement Lm-XFEM. The numerical results of the SIFs estimated based on the two given sets of children elements are then shown in Fig. 25. Similarly, the common XFEM with fine mesh and exact solutions [60] are also plotted in the same figure for the validation purpose. The present results indicate clearly that the Lm-XFEM with $5 \times 5 \times 5$ subdivision elements can offer a good accuracy as their SIFs are closer to the exact solutions than other reference solutions. However, the cost that devotes to the use of a higher number of subdivision elements is high.

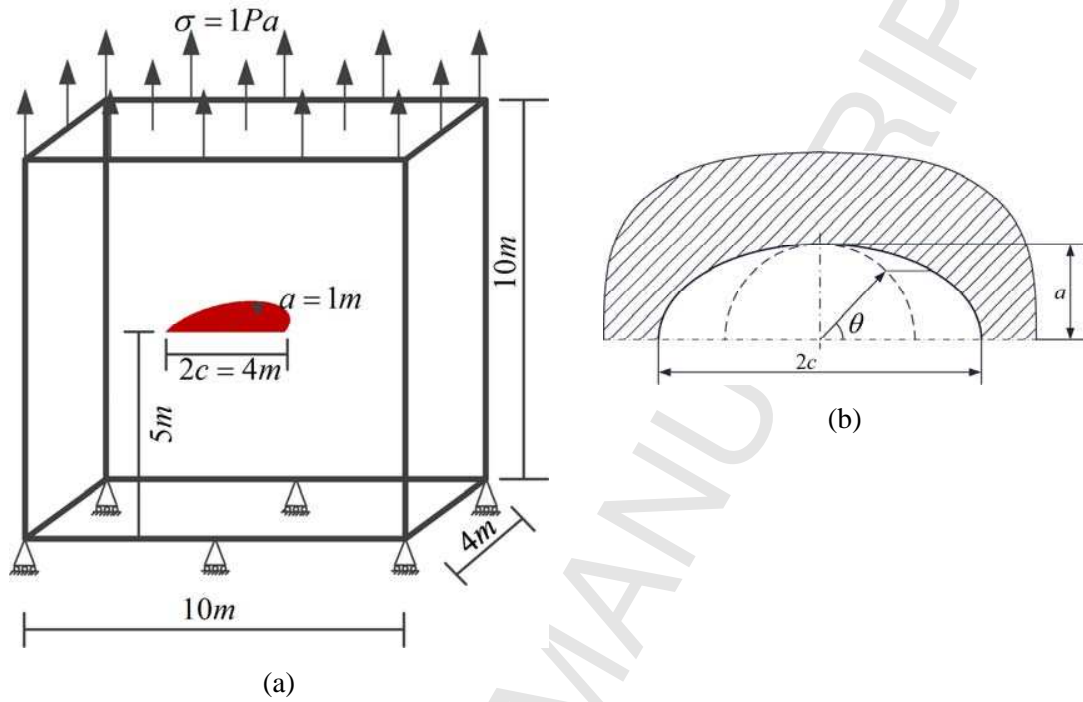


Fig. 23 Geometric notation of an edge ellipse shaped crack in finite domain and its configuration parameters (a); and close-up of crack and angle (b).

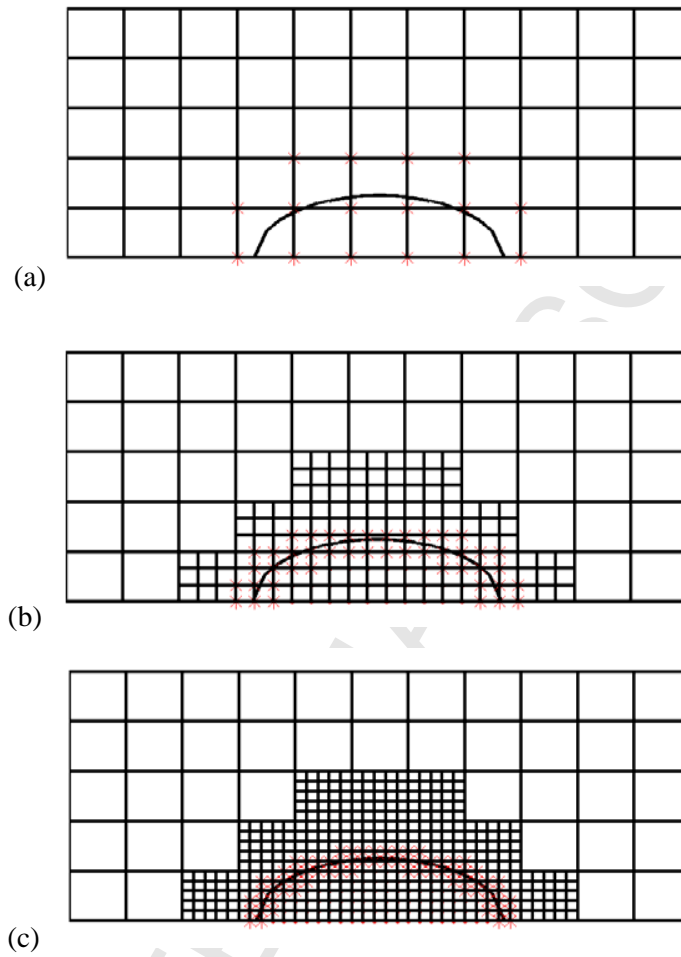


Fig. 24 Top-side views of cross-section of an edge ellipse shaped crack in finite domain: initial mesh (a) ; a $3 \times 3 \times 3$ refined Lm-XFEM mesh (b) and a $5 \times 5 \times 5$ refined Lm-XFEM mesh (c)

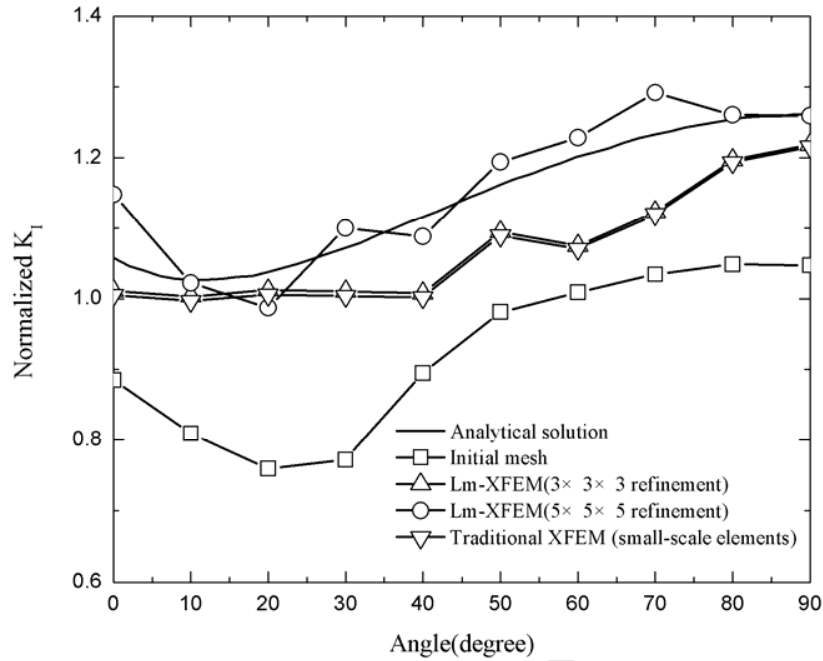


Fig. 25 Comparison of the normalized stress intensity factor (mode-I) at different angles along the crack front for an edge ellipse shaped crack among the Lm-XFEM, the conventional XFEM and the exact solution.

5. Conclusions and outlook

A novel 3-D adaptive local mesh refinement extended finite element method (Lm-XFEM) using hexahedron elements for the accurate computation of the stress intensity factors of planar straight and curved cracks in solids is presented. This 3-D approach, on one hand, engages a *posteriori* recovery-based error estimation to detect all elements that shall be refined in the next refinement step, the variable-node hexahedron elements, on the other hand, are adopted to treat the mismatching problems caused by different scale-meshes. The strategy presenting here reflects the robustness of an effective numerical method as the fine-scale mesh is only tackled to where it is required. The numerical results of the SIFs for single and mixed-mode 3-D crack problems obviously show the effectiveness and high accuracy of the proposed Lm-XFEM method.

We have found through the numerical investigation that the variable-node hexahedron element based on the generic point interpolation is effective and straightforward in treating the

mismatching problems of different meshes. The adaptive algorithm reflects the region where fine meshes are required to be refined, which makes the method possible to improve the accuracy of the solutions around the cracks. Moreover, the Lm-XFEM carries with less DOFs than those through the XFEM.

In XFEM setting, the mesh is independent of crack geometry, and small cracks in the analysis of large structures can be considered by employing the coupling meshes scheme. The Lm-XFEM proposed thus is an efficient numerical method, and is particularly suitable for modeling cracks embedded in large structures. Due to the accuracy, simplicity, and the flexibility of the Lm-XFEM, we believe that the method presented here is well and ideally suited for engineering analysis. The proposed formulation is general and its extension to other complex problems is possible. Multiple cracks, crack growth in 3-D problems, and non-planar 3-D cracks are those that are very interesting to study. We may further develop it for modeling cracks in advanced composite materials, e.g., layered functionally graded materials [51], or to industrial applications problems. Those works inherently are challenging but would be an interesting subject for our future research directions.

More specifically, the multiple branched cracks can be modelled by introducing a junction function to the present displacement approximation. The presented formulas in this paper can be further developed for solving non-planar 3-D cracks as well. In the XFEM, the crack surface is often described through the level sets. Compared with planar 3-D cracks, representing non-planar 3-D cracks with the level set method would be more complicated. The crack growth in 3-D problems can be modelled by introducing appropriate crack propagation criteria into the present formulation. The high-efficient updating algorithm of level sets and 3-D crack growth algorithm are two key issues in the analysis of 3-D crack propagation. Some scholars successfully modelled 3-D crack propagation with the XFEM, see for instance Refs. [42, 61].

In addition, the discretization of tetrahedral elements is common in general engineering practice. The variable-node tetrahedral elements can be devised based on the generic point interpolation with an arbitrary number of nodes on each of their faces, thus the proposed method can be applied to complex problems discretized with tetrahedral elements.

Nonetheless, the current version of the developed 3-D Lm-XFEM employs the displacement extrapolation method to extract the SIFs. As have been shown in the subsequent

numerical examples, the current version works quite well for both straight and curved cracks as well as single and mixed-mode fractures. Further development by taking the M-integral method and integrating it into the Lm-XFEM is necessary and important. To this end, the accuracy of the SIFs and the path independent problem are two important issues that must be taken into consideration.

Acknowledgements

This work was supported by the Grant-in-Aid for Scientific Research - Japan Society for the Promotion of Sciences (JSPS); the National Natural Science Foundation of China (Grant No. 51179063); and the National Sci-Tech Support Plan of China (Grant No. 2015BAB07B10). The financial supports are gratefully acknowledged.

References

- [1] P.A. Guidault, O. Allix, L. Champaney, J.P. Navarro, A two-scale approach with homogenization for the computation of cracked structures, *Computers and Structures* 85(2007)1360-1371.
- [2] M. Holl, S. Loehnert, P. Wriggers, An adaptive multiscale method for crack propagation and crack coalescence, *Internat. J. Numer. Methods Engrg.* 93(2013)23-51.
- [3] C. Prange, S. Loehnert, P. Wriggers, Error estimation for crack simulations using the XFEM, *Internat. J. Numer. Methods Engrg.* 91(2012)1459-1474.
- [4] P.A. Guidault, Q. Allix, L. Champaney, C. Cornuault, A multiscale extended finite element method for crack propagation, *Comput. Methods Appl. Mech. Engrg.* 197(2008)381-399.
- [5] S. Loehnert, T. Belytschko, A multiscale projection method for macro/microcrack simulations, *Internat. J. Numer. Methods Engrg.* 71(2007)1466-1482.
- [6] A. de Boer, A.H. van Zuijlen, H. Bijl, Review of coupling methods for nonmatching meshes, *Comput. Methods Appl. Mech. Engrg.* 196(2007)1515-1525.
- [7] M.A. Puso, A 3D mortar method for solid mechanics, *Internat. J. Numer. Methods Engrg.* 59(2002)315-336.
- [8] H.B. Dhia, G. Rateau, The Arlequin method as a flexible engineering design tool, *Internat. J.*

- Numer. Methods Engrg. 62(2005)1442-1462.
- [9] T. Belytschko, S. Loehnert, J.H. Song, Multiscale aggregating discontinuities: A method for circumventing loss of material stability, *Internat. J. Numer. Methods Engrg.* 73(2008)869-894.
- [10] N. Moës, J. Dolbow, T. Belytschko, A finite element for crack growth without remeshing, *Internat. J. Numer. Methods Engrg.* 46(1999)131-150.
- [11] J.H. Song, T. Belytschko, Multiscale aggregating discontinuities method for micro–macro failure of composites, *Composites Part B: Engineering* 40(2009)417-426.
- [12] T. Belytschko, J.H. Song, Coarse-graining of multiscale crack propagation, *Internat. J. Numer. Methods Engrg.* 81(2010)537-563.
- [13] J.A. Plews, C.A. Duarte, Bridging multiple structural scales with a generalized finite element method, *Internat. J. Numer. Methods Engrg.* 102(2015)180-201.
- [14] T. Hettich, A. Hund, E. Ramm, Modeling of failure in composites by X-FEM and level sets within a multiscale framework, *Comput. Methods Appl. Mech. Engrg.* 197(2008)414-424.
- [15] E. Pierrès, M.C. Baietto, A. Gravouil, A two-scale extended finite element method for modelling 3D crack growth with interfacial contact, *Comput. Methods Appl. Mech. Engrg.* 199(2010)1165-1177.
- [16] A. Sarhangi Fard, M.A. Hulsen, H.E.H. Meijer, N.M.H. Famili, P.D. Anderson, Adaptive non-conformal mesh refinement and extended finite element method for viscous flow inside complex moving geometries, *International Journal for Numerical Methods in Fluids* 68(2012)1031-1052.
- [17] A. Byfut, A. Schröder, hp-adaptive extended finite element method, *Internat. J. Numer. Methods Engrg.* 89(2012)1392-1418.
- [18] S. Loehnert, C. Prange, P. Wriggers, Error controlled adaptive multiscale XFEM simulation of cracks, *International Journal of Fracture* 178(2012)147-156.
- [19] D. Sohn, J.H. Lim, S. Im, An efficient scheme for coupling dissimilar hexahedral meshes with the aid of variable-node transition elements, *Advances in Engineering Software* 65(2013)200-215.
- [20] S. Kumar, I.V. Singh, B.K. Mishra, A homogenized XFEM approach to simulate fatigue crack growth problems, *Computers and Structures* 150 (2015) 1-22

- [21] S. Kumar, I.V. Singh, B.K. Mishra, T. Rabczuk. Modeling and simulation of kinked cracks by virtual node XFEM, *Computer Methods in Applied Mechanics and Engineering*. 283(2015)1425-1466.
- [22] J.H. Lim, D. Sohn, S. Im, Variable-node element families for mesh connection and adaptive mesh computation, *Structural Engineering and Mechanics* 43(2012)349-370.
- [23] Q.T. Bui, Ch. Zhang, Extended finite element simulation of stationary dynamic cracks in piezoelectric solids under impact loading, *Computational Materials Science* 62(2012)243-257.
- [24] Q.T. Bui, Ch. Zhang, Analysis of generalized dynamic intensity factors of cracked magneto-electroelastic solids by X-FEM, *Finite Elem. Anal. Des.* 69(2013)19-36.
- [25] P. Liu, T.T. Yu, Q.T. Bui, Ch. Zhang, Transient dynamic crack analysis in non-homogeneous functionally graded piezoelectric materials by the X-FEM, *Computational Materials Science* 69(2013)542-558.
- [26] P. Liu, T.T. Yu, Q.T. Bui, Ch. Zhang, Y.P. Xu, C.W. Lim, Transient thermal shock fracture analysis of functionally graded piezoelectric materials by the extended finite element method, *International Journal of Solids and Structures* 51(2014)2167-2182.
- [27] T.T. Yu, Q.T. Bui, P. Liu, Ch. Zhang, S. Hirose, Interfacial dynamic impermeable cracks analysis in dissimilar piezoelectric materials under coupled electromechanical loading with the extended finite element method, *International Journal of Solids and Structures*, 67-68(2015)205-218.
- [28] K. Sharma, Q.T. Bui, Ch. Zhang, R.R. Bhargava, Analysis of a subinterface crack in piezoelectric bimaterials with the extended finite element method, *Engineering Fracture Mechanics* 104(2013)114-139.
- [29] S. Bhattacharya, I.V. Singh, B.K. Mishra, Q.T. Bui, Fatigue crack growth simulations of interfacial cracks in bi-layered FGMs using XFEM, *Comput. Mech.* 52(2013)799-814.
- [30] X.D. Zhang, Q.T. Bui, A fictitious crack XFEM with two new solution algorithms for cohesive crack growth modeling in concrete structures, *Engineering Computations* 32(2015)473-497.
- [31] T.T. Yu, Q.T. Bui, P. Liu, S. Hirose, A stabilized discrete shear gap extended finite element for the analysis of cracked Reissner-Mindlin plate vibration problems involving

- distorted mesh, *International Journal of Mechanics and Materials in Design* 12 (2016) 85-107.
- [32] P. Liu, T.Q. Bui, D. Zhu, T.T. Yu, J.W. Wang, S.H. Yin, S. Hirose, Buckling failure analysis of cracked functionally graded plates by a stabilized discrete shear gap extended 3-node triangular plate element. *Composites Part B: Engineering* 77 (2015) 179-193.
- [33] L. Shi, T.T. Yu, T.Q. Bui, Numerical modeling of hydraulic fracturing in rock mass by XFEM. *Soil Mechanics and Foundation Engineering* 52 (2015) 74-83.
- [34] Z. Kang, T.Q. Bui, D.D. Nguyen, T. Saitoh, S. Hirose, An extended consecutive-interpolation quadrilateral element (XCQ4) applied to linear elastic fracture mechanics *Acta Mechanica* 226 (2015) 3991-4015.
- [35] H. Pathak, A. Singh, I.V. Singh, S. K. Yadav, A simple and efficient XFEM approach for 3-D cracks simulations, *International Journal of Fracture*. 181(2013) 189-208.
- [36] H. Pathak, A. Singh, I.V. Singh, S. K. Yadav, Fatigue crack growth simulations of 3-D linear elastic cracks under thermal load by XFEM, *Frontiers of Structural and Civil Engineering*, 9(2015)359-382.
- [37] H. Pathak, A. Singh, I.V. Singh, Fatigue crack growth simulations of 3-D problems using XFEM, *International Journal of Mechanical Sciences* 76(2013)112-131.
- [38] K. Sharma, I.V. Singh, B.K. Mishra, S.K. Maurya, Numerical Simulation of Semi-elliptical axial crack in pipe bend using XFEM, *Journal of Solid Mechanics* 6(2014) 208-228.
- [39] O.C. Zienkiewicz, J.Z. Zhu. A simple error estimator and adaptive procedure for practical engineering analysis. *Internat. J. Numer. Methods Engrg.* 24 (1987) 337-357.
- [40] N. Sukumar, N. Moës, B. Moran, T. Belytschko, Extended finite element method for three-dimensional crack modeling, *Internat. J. Numer. Methods Engrg.* 48(2000)1549-1570.
- [41] L.S. Chen, J.H. Kuang, A modified linear extrapolation formula for determination of stress intensity factors, *International Journal of Fracture* 54(1991)R3-R8.
- [42] N. Moës, A. Gravouil, T. Belytschko, Non-planar 3D crack growth by the extended finite element and level sets—Part I: Mechanical model, *Internat. J. Numer. Methods Engrg.* 53(2002)2549-2568.
- [43] P. Laborde, J. Pommier, Y. Renard, M. Salaün, High order extended finite element

- method for cracked domains, *Int. J. Numer. Meth. Engng.* 64(2005)354-381.
- [44] T.P. Fries, A corrected XFEM approximation without problems in blending elements, *Int. J. Numer. Meth. Engng.* 75(2008)503-532.
- [45] E. Chahine, P. Laborde, Y. Renard, Crack tip enrichment in the XFEM using a cutoff function, *Int. J. Numer. Meth. Engng.* 75(2008)629-646.
- [46] R. Gracie, H. Wang, T. Belytschko, Blending in the extended finite element method by discontinuous Galerkin and assumed strain methods, *Int. J. Numer. Meth. Engng.* 74(2008) 1645-1669.
- [47] J.E. Tarancón, A. Vercher, E. Giner, F.J. Fuenmayor, Enhanced blending elements for XFEM applied to linear elastic fracture mechanics, *Int. J. Numer. Meth. Engng.* 77(2009) 126-148.
- [48] J. Chessa, H. Wang, T. Belytschko, On the construction of blending elements for local partition of unity enriched finite elements, *Int. J. Numer. Meth. Engng.* 57(2003)1015-1038.
- [49] D.M. Parks, A stiffness derivative finite element technique for determination of crack tip stress intensity factors, *International Journal of Fracture Mechanics* 10(1974)487-502.
- [50] E.F. Rybicki, M.F. Kanninen, A finite element calculation of stress intensity factors by a modified crack closure integral, *Engineering Fracture Mechanics* 9(1977)931-938.
- [51] M. Gosz, B. Moran, An interaction energy integral method for computation of mixed-mode stress intensity factors along non-planar crack fronts in three dimensions, *Engineering Fracture Mechanics* 69(2002)299-319.
- [52] V.F. González-Albuixech, E. Giner, J.E. Tarancón, F.J. Fuenmayor, A. Gravouil, Convergence of domain integrals for stress intensity factor extraction in 2-D curved cracks problems with the extended finite element method, *Internat. J. Numer. Methods Engrg.* 94(2013)740-757.
- [53] T.L. Anderson, *Fracture Mechanics, Fundamentals and Applications* (Second edition). CRC press, New York, 1995.
- [54] H. Liebowitz, G.C. Sih. *Mathematical Theories of Brittle Fracture*. Academic Press, New York, 1968.
- [55] D. Xie, Q. Qian, C.A. Li, *Numerical calculation method and engineering application in*

fracture mechanics, Beijing: China Science Press,2009.

- [56] H. Tada, P.C. Paris, R. Irwin, The stress analysis of cracks (Handbook), Del Research Corporation, Hellertown, Pennsylvania,1973.
- [57] Institute of China Aeronaut, Handbook of stress intensity factors (Revised Edition), Science Press, Beijing,1993.
- [58] A.E. Green, I.N. Sneddon, The distribution of stress in the neighbourhood of a flat elliptical crack in an elastic solid, Math Proc Camb Philos Soc 46(1950)159-163.
- [59] G.R. Irwin, The crack extension force for a part-through crack in a plate. ASME, Journal of Applied Mechanics 29(1962)651-654.
- [60] J.C. Newman Jr., I.S. Raju, Stress-intensity factor equations for cracks in three-dimensional finite bodies subjected to tension and bending loads, In: Atluri, S. (Ed.), Computational Methods in the Mechanics of Fracture, Computational methods in mechanics, vol. 2. Elsevier Science Publishers, Amsterdam, 1986, 311-334.
- [61] P.M.A. Areias, T. Belytschko, Analysis of three-dimensional crack initiation and propagation using the extended finite element method, Int. J. Numer. Meth. Engng 63(2005)760-788.